January 2008

Metallic Carbon Nanotubes, Microwave Characterization And Development Of A Terahertz Detector

Kan Fu
University of Massachusetts Amherst

METALLIC CARBON NANOTUBES, MICROWAVE CHARACTERIZATION AND DEVELOPMENT OF A TERAHERTZ DETECTOR

A Thesis Presented

by

Kan Fu

Submitted to the Graduate School of the
University of Massachusetts Amherst in partial fulfillment
of the requirements for the degree of

Master of Science in Electrical and Computer Engineering

May 2008

Electrical and Computer Engineering

METALLIC CARBON NANOTUBES, MICROWAVE CHARACTERIZATION AND DEVELOPMENT OF A TERAHERTZ DETECTOR

A Thesis Presented

by

Kan Fu

Approved as to style and content by:

K.Sigfrid Yngvesson, Chair

Eric Polizzi, Member

Marinos Vouvakis, Member

C. V. Hollot, Department Head
Electrical and Computer Engineering

I dedicate this thesis to my parents

ACKNOWLEDGMENTS

The finishing of this thesis is a wonderful learning experience for me. I feel really grateful to so many people that involved in the work of this thesis.

Firstly, I would like to thank my advisor, Professor K. S. Yngvesson, who gives me great help and constant guidance all the way along this thesis work. Without his professional guidance and encouragement, the finish of this thesis will never happen. His broad knowledge in Terahertz, Semiconductor electronics and Microwave gives me the best opportunity to combine these knowledge into my understanding of the work. I also appreciate his help during my experiments. I will always remember the midnight of May 18, 2007, when we first got terahertz detection on carbon nanotubes.

I also want to thank the members of the committee, Professor Eric Polizzi and Professor Marinos Vouvakis. They are best teachers I met at UMass, I learned a lot semiconductor physics and computational electromagnetics in their classes. I really appreciate their precious time the suggestions on the thesis.

I wish to thank my colleagues, my teachers and my friends. I learned a lot and got great help and encouragements from them. It is a great experience to work with them. Dr. Fernando Rodriguez-Morales taught me the operations of all sorts of terahertz and microwave equipments and other lab works. He is so kind to offer me the help even after he left Terahertz Lab. Ric Zannoni taught me the operations of the lasers, and he is very helpful whenever I met a problem. Special thanks to John Nicholson, he offered me a lot of assistances and guidances in the lab during this work, and he fabricated all the semiconductor devices used in this thesis. Chak Chan helped me a lot in my experiments. Dr. Dazhen Gu gave me many useful suggestions from Boulder, Colorado. I would like to thank Professor Robert W. Jackson for allowing me to use their equipments. I would also like to thank to the help of Dr. Nidhi Khandelwal and Mauricio Sanchez from LAMMDA and the help of Ozgur Yavuzcetin from Physics Department for taking AFM pictures. Additionally,

I would like to thank the collaboration of Bo Fu, Alex de Geofroy, Stephan Adams, Amine Ouarraoui and Jason Donovan.

Finally, I would like to thank my parents, for their encouragement and support.

TABLE OF CONTENTS

Page

LIST OF TABLES . . . . . **x**

LIST OF FIGURES . . . . . **xi**

CHAPTER

1. INTRODUCTION **1**

1.1 Overview of Nanoelectronics 1
1.2 Carbon Nanotube Basics 2

1.2.1 Metallic Single-Walled Carbon Nanotubes 4
1.2.2 Theory of high frequency detectors 7

1.2.2.1 The diode mode 8
1.2.2.2 The bolometer mode 9
1.2.2.3 Photon-assisted Tunneling 10

1.2.3 Possible application of SWCNTs as terahertz and microwave detectors 11

1.3 Scope of this Work 13
1.4 Organization of the Thesis 14

2. EXPERIMENTS **15**

2.1 Terahertz Measurements 15

2.1.1 Device Preparation and Configuration 15
2.1.2 Experimental Setups 20

2.1.2.1 Terahertz source 22
2.1.2.2 DC biasing 23
2.1.2.3 Temperature sensor 24

2.1.3 Results 24

2.1.3.1 DC results . . . 24
2.1.3.2 Terahertz detection results . . . 25
2.1.3.3 Results of measurements regarding temperature dependence . . . 28

2.2 Microwave Measurements . . . 34

2.2.1 Device configurations . . . 34
2.2.2 Experimental Setups . . . 34
2.2.3 Results . . . 36

2.2.3.1 DC results . . . 36
2.2.3.2 Microwave detection . . . 38
2.2.3.3 S-parameter measurement . . . 38

3. PHYSICAL PROCESS OF THE DETECTION . . . 45

3.1 Terahertz detection process modeling . . . 45

3.1.1 Bolometer Model . . . 45

3.2 Microwave data analysis . . . 62

3.2.1 De-embedding process . . . 62
3.2.2 De-embedding results . . . 63
3.2.3 Circuit model . . . 63

3.3 Consequences of the circuit model for the terahertz detection process . . . 72

3.3.1 Terahertz absorption in the CNTs . . . 72
3.3.2 Mechanism of the change of the resistance . . . 73

4. FUTURE WORK . . . 75

4.1 Terahertz detection . . . 75

4.1.1 Detections on the short-gap antenna . . . 75
4.1.2 Detection on Suspended SWNTs . . . 76
4.1.3 Heterodyne detection on SWNTs . . . 76

4.2 Microwave measurements . . . 77

4.2.1 More accurate on-wafer microwave measurements and de-embedding method . . . 78
4.2.2 Microwave probe measurements at cryogenic temperatures . . . 78

APPENDIX: CALCULATIONS OF THERMAL CONDUCTANCE AND HEAT CAPACITY **79**

BIBLIOGRAPHY **81**

LIST OF TABLES

Table **Page**

1.1 Comparison between different high-frequency detectors 13

2.1 Devices tested in this thesis work 18

2.2 Summary of common laser lines used in this investigation. 23

2.3 Devices tested in the microwave measurements 35

3.1 The principal types of far infrared detectors 46

3.2 Values of G_{th} obtained at different temperatures and frequencies 52

3.3 Extracted values of the lumped elements in the circuit model. 68

LIST OF FIGURES

Figure **Page**

1.1 Shown here are a (5, 5) armchair nanotube (top), a (9, 0) zigzag nanotube (middle) and a (10, 5) chiral nanotube[33]. 3

1.2 (a) The lattice structure of graphene, a honeycomb lattice of carbon atoms. (b) The energy of the conducting states as a function of the electron wavevector k. There are no conducting states except along special directions where cones of states exist. (c), (d) Graphene sheets rolled into tubes. This quantizes the allowed k values around the circumferential direction, resulting in 1D slices through the 2D band structure in (b). Depending on the way the tube is rolled up, the result can be either a metal (c) or a semiconductor (d).Ref.[30] 3

1.3 The circuit model of a non-contacted nanotube, the cell repeats periodically, Ref.[41]. 5

1.4 The circuit model of a contacted nanotube. 6

1.5 (a)Proposed circuit model for the SWCNT. (b)Results of fitting the circuit model to the measured CNT impedance data as a function of frequency with and without L_K. (c)Result of fitting the circuit model to the measured CNT phase angle data as a function of frequency with and without L_K, Ref.[46] 7

1.6 Alternative dc equivalent circuits of a microwave detector device, Ref[50]. 9

1.7 The heat flow diagram of the bolometer. 11

1.8 Experimental verification of FET operation at frequencies up to 23 GHz. The carbon nanotube FET amplifier is operated with an input signal containing two tones, at frequencies f and f +10 kHz. The FET acts like a mixer, producing an intermodulation product at 10 kHz. The amplitude of the 10 kHz output signal is plotted as a function of input frequency. We see no evidence of a rolloff caused by the CNT FET, even at 23 GHz, Ref[58]. 12

1.9 Diagram of SWNT network suspended between electrical contacts, Ref[60]. 12

2.1 Microscope picture of a planar log-periodic antenna. 16

2.2 Diagram of the metal and semiconductor layers 17

2.3 Diagram of the setup of the DEP process. 17

2.4 Photograph of the backside of the chip with the silicon lens. 19

2.5 The functional description of the detection block. 19

2.6 The detection block and the wire bonded chip. 20

2.7 Photograph of the liquid helium dewar. 21

2.8 The diagram of the experimental setup. 22

2.9 Photograph of the CO_2-pumped far infrared (FIR) laser used as THz source. 23

2.10 Diagram of the silicon diode temperature sensor. 24

2.11 I-V curve of device A at room temperature (left) and at 77 K (right). 25

2.12 I-V curve of device B1 at room temperature (left) and at 77 K (right). 25

2.13 I-V curve of device B2 at room temperature (upper left), 77 K (upper right) and 4.23 K (bottom). 26

2.14 Terahertz detection results for device A(black dots, left scale) and comparison with results from diode model(red curves, right scale). 27

2.15 Responsivities of terahertz detection of Device B1(black dots, left scale) and comparison with diode mode data(red curves, right scale). 29

2.16 Responsivities of terahertz detection of Device B2(black dots, left scale)compared with the diode mode data(red curves, right scale). 30

2.17 Summaries of the responsivities of the terahertz detection. 31

2.18 I-V curve of device B2 at different temperatures. 31

2.19 Terahertz detection on device B2 as a function of the temperature both in linear scale (left) and log scale (right). 32

2.20 Resistances of device B2 as a function of the temperature both in linear scale (left) and log scale (right). 33

2.21 Photograph of the co-planar waveguide structure. 35

2.22 Diagram of the microwave measurement setups. 36

2.23 DC results of different devices. 37

2.24 Microwave detection as a function of bias voltage of different devices(black dots, left scale) and the diode mode data(red curves, right scale). 39

2.25 Microwave detection as a function of microwave frequency of different devices. 40

2.26 Microwave detection as a function of microwave power level of different devices. 41

2.27 Magnitude of S11 of different devices. 43

2.28 The S11 parameter of different devices on smith chart. 44

3.1 Diagram of the thermal bolometer detector. 46

3.2 Resistances of device B2 as a function of bias voltage at different temperatures. 50

3.5 The temperature coefficient of device B2 as a function of bias voltage at different temperatures. 50

3.3 Resistances of device B2 as a function of the temperature both in linear scale (top) and log scale (bottom). 51

3.4 dR/dT of device B2 as a function of bias voltage at different temperatures. 52

3.6 Comparison between the experimental data and the bolometer model data at 0.694THz, 4.23K. 53

3.7 Comparison between the experimental data and the bolometer model data at 1.05THz, 4.23K. 53

3.8 Comparison between the experimental data and the bolometer model data at 1.63THz, 4.23K. 54

3.9 Comparison between the experimental data and the bolometer model data at 2.54THz, 4.23K. 54

3.10 Comparison between the experimental data and the bolometer model data at 1.40THz, 4.23K. 55

3.11 Comparison between the experimental data and the bolometer model data at 1.40THz, room temperature. 55

3.12 The T-dependence of the thermal conductance G_{th}. 57

3.13 Responsivity with device B2 as a function of the temperature both in linear scale (up) and log scale (bottom). 58

3.14 Measured responsivity of device B2 vs. the modulation frequency. 60

3.15 The FIR response versus modulation frequency of the THz laser in our lab[95]. 61

3.16 Schematic of the microwave probe with the CPW structure. 62

3.17 Circuit model of the CPW structure with(left) and without DUT(right). 63

3.18 De-embedded impedance of CNTs in device C. 64

3.19 De-embedded impedance of CNTs in device D. 64

3.20 De-embedded impedance of CNTs in device E1. 65

3.21 De-embedded impedance of CNTs in device F. 65

3.22 The circuit model used in this work to fit the de-embedded data. 65

3.23 De-embedded impedance versus frequency with the circuit fits of CNTs in device C. 66

3.24 De-embedded impedance versus frequency with the circuit fits of CNTs in device D. 66

3.25 De-embedded impedance versus frequency with the circuit fits of CNTs in device E1. 67

3.26 De-embedded impedance versus frequency with the circuit fits of CNTs in device F. 67

3.27 The normalized contacts voltage versus frequency of device C predicted by the circuit model. 69

3.28 The normalized contacts voltage versus frequency of device D predicted by the circuit model. 70

3.29 The normalized contacts voltage versus frequency of device E1 predicted by the circuit model. 70

3.30 The normalized contacts voltage versus frequency of device F predicted by the circuit model. 71

3.31 The normalized contacts voltage of different devices. 71

3.32 Simulation of S11 for a TL model of a ten tube m-SWNT bundle. The contact resistances are assumed to be shorted by the contact capacitances 73

4.1 The photograph of the 1-μm gap mask. 76

4.2 Diagram of the suspended tubes, Ref[100]. 77

CHAPTER 1

INTRODUCTION

1.1 Overview of Nanoelectronics

The huge success of microelectronics and the semiconductor industry was largely fueled by the scalability of the planar MOSFET. However, with the feature size of CMOS transistors down below 100 nm, the devices, the transistors themselves, are not performing better just because they are scaled smaller. They may actually perform worse at the smallest scales. One has to incorporate new ideas, new materials, and new structures to keep performance and miniaturization on the same pace as past decades [1]. Intensive research have been done focusing on the possible options to extend microelectronics into nanoelectronics. The National Science Foundation defines nanotechnology as work at the 1-100 nm length scale to produce structures, devices, and systems that have novel properties because of their nanoscale dimensions [2]. The research on nanoelectronics lies in two main categories: new structures, and new materials to improve the performance of the conventional field effect transistor(FET); the other is completely different transistors. The former includes high-$\mathcal{K}$ dielectrics [3], [4], silicon-on-insulator(SOI) [5], the multigate field effect transistor(MuGFET) [6], [7], and the carbon nanotube field effect transistor(CNTFET) [8]–[13]; The latter includes the single electron transistor(SET) [14]–[21], the molecular transistor [11], [22]–[25], the spin transistor [26] and quantum cellular automata(QCA) [27].

This thesis focuses on the characterizations of single wall carbon nanotubes(SWNTs) at terahertz and microwave frequencies.

1.2 Carbon Nanotube Basics

Although there is still controversy over the discovery of carbon nanotubes [28], a large percentage of the academic and popular literature attributes the discovery of hollow, nanometer sized tubes composed of graphitic carbon to *S. Iijima* of NEC in 1991 [29].

Carbon nanotubes can be viewed as a sheet of graphene rolled up into a seamless cylinder [30], [31]. There are two main types of carbon nanotubes, multi-walled nanotubes(MWNTs) and single-walled nanotubes(SWNTs). MWNTs contain overlapping cylindrical tubes, like a coaxial cable. Their typical diameters range from a few nanometers to around 100 nm [32], depending on the number of concentric tubes. SWNTs, on the other hand, consist of one tube with diameters typically from 0.5 nm to 3 nm.

The electrical properties of carbon nanotubes are dependent on their chiralities and diameters. The chirality of a carbon nanotube is determined by its so called chiral vector $\vec{C} = n\vec{a_1} + m\vec{a_2}$, which defines the direction in which the graphene sheet may be wrapped, in other words, which is the circumferential direction of the carbon nanotube. Based on different combinations of n and m, carbon nanotubes can be sorted into three main types: 1)when n = m, the CNT is an armchair structure; 2) when m = 0, the CNT is a zigzag structure. 3)Otherwise, the CNT is called "chiral" [33]. The band structures of CNTs are dependent on the values of n and m as well as the values of their diameters. All armchair tubes are metallic. If the difference between n and m, $|n-m|$, is a multiple of 3, then the zigzag and chiral CNTs are quasi-metallic, with a very small bandgap (a few meV) compared to typical semiconductors'. All other CNTs are semiconducting [30].

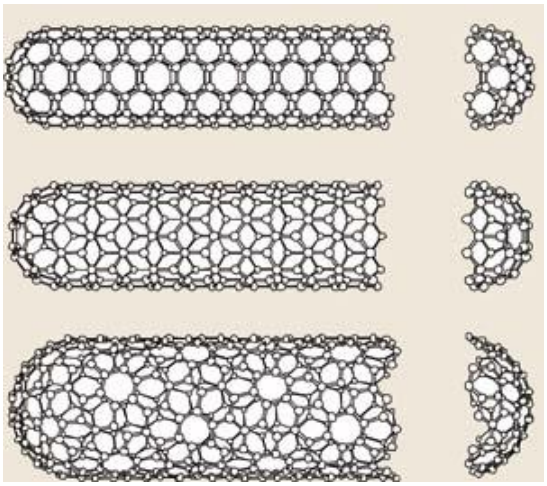

Figure 1.1. Shown here are a (5, 5) armchair nanotube (top), a (9, 0) zigzag nanotube (middle) and a (10, 5) chiral nanotube[33].

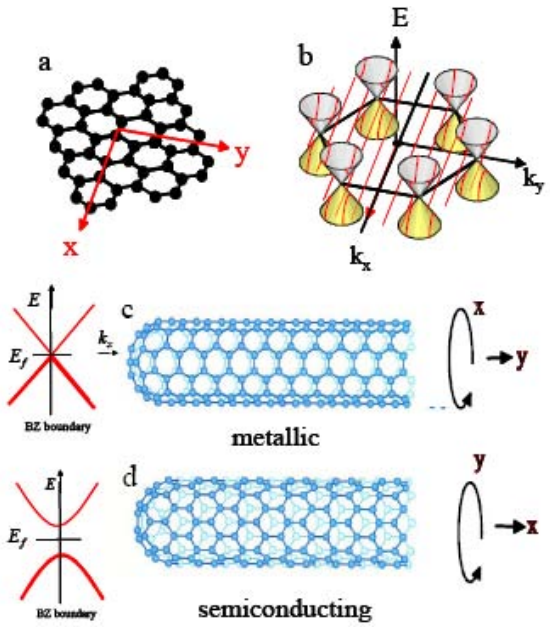

Figure 1.2. (a) The lattice structure of graphene, a honeycomb lattice of carbon atoms. (b) The energy of the conducting states as a function of the electron wavevector k. There are no conducting states except along special directions where cones of states exist. (c), (d) Graphene sheets rolled into tubes. This quantizes the allowed k values around the circumferential direction, resulting in 1D slices through the 2D band structure in (b). Depending on the way the tube is rolled up, the result can be either a metal (c) or a semiconductor (d).Ref.[30]

1.2.1 Metallic Single-Walled Carbon Nanotubes

Devices made from metallic SWNTs (m-SWCNTs) were first measured in 1997 [34], [35], and have been extensively studied since that time. When one applies a dc voltage across a SWNT, the electrons will move along the tube and generate a dc current. However, the picture here is quite different from a normal bulk metal conductor due to the 1-D property of nanotubes.

Recent work has shown that the mean free paths (mfp) for optical phonon scattering and acoustic phonon scattering in m-SWCNTs, respectively, are 15nm and >1um at room temperature [36]–[38]. As the temperature is decreasing, the acoustic phonon mean free path(mfp) becomes longer. Also, optical phonon scattering does not occur for low energy electrons, i.e. low bias voltage, <0.2V. The mfp for impurity/defect scattering depends on the tube quality and can be several micrometers. Thus the metallic SWNTs exhibit a quasi-ballistic conduction. In the ideal case, i.e. perfect contacts, the maximum conductance is predicted by Landauer formula [39] to be Ne^2/h, where N is the number of conducting modes at the *Fermi* energy. There are two modes if we take spin into account. Also, there is a degeneracy of two as can be seen in Figure 1.2c. With N=4, the minimum resistance then becomes 6.47 kΩ, for ballistic nanotubes. The measured two-terminal resistances of metallic SWNTs at room temperature can vary significantly, ranging from as small as ∼6kΩ to several megaohms(MΩ) [30]. Most of this variation is due to variations in contact resistance between the electrodes and the tube [30]. The shapes of the I-V curve of the CNTs are also dependent on the contact resistance [40].

The ac transport properties of metallic CNTs are also influenced by the 1-D structure of the CNTs. The circuit model of the gigahertz electrical properties of carbon nanotubes was developed by Burke [41] using the Lüttinger liquid theory. The low density of states in 1-D conductors compared with the 3-D case means that one has to consider the extra kinetic energy that must be added when electrons are placed

in conducting states - this effect is inductive and can be described by a "kinetic inductance (L_K)" in an equivalent circuit. Likewise, electrostatic energy has to be added, and this results in a "quantum capacitance (C_Q)" in series with the usual electrostatic capacitance (C_E). For a metallic SWNT, L_K (16nH/μm in the single mode case, and 4nH/μm for N=4) is typically more than three orders of magnitude greater than the standard electromagnetic inductance L_M associated with building up the stored magnetic energy, and L_M can be neglected. C_E is of the same magnitude as C_Q ($\sim$100aF/μm) [41]. Based on the discussions above, a circuit model for a non-contacted carbon nanotube can be obtained, shown in Figure 1.3.

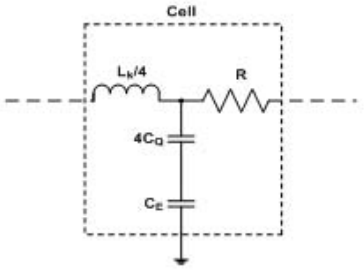

Figure 1.3. The circuit model of a non-contacted nanotube, the cell repeats periodically, Ref.[41].

The complete model of the metallic CNT actually consists of four parallel transmission lines representing four possible modes of propagation. Three of these modes are so-called spin modes and do not transport charge. The fourth mode does transport charge and is called the charge mode. In this proposed thesis, we are only concerned about the charge mode. For this mode, L_K is divided by four and C_Q is multiplied by four, whereas C_E stays unchanged. To do carbon nanotube measurements, electrodes are needed to contact the nanotubes. Thus, additional circuit elements need to be added to the transmission line model, shown in Fig. 1.4. From the transmission line model in the previous section, the phase velocity V_p and the characteristic impedance Z_C of the transmission line can also be derived as follows:

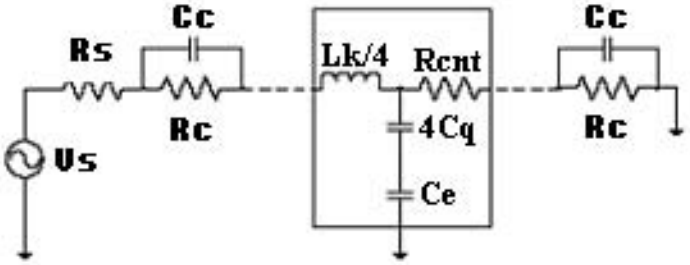

Figure 1.4. The circuit model of a contacted nanotube.

$$v_p = \frac{1}{\sqrt{L_K C_{tot}}} = v_F \sqrt{1 + \frac{4C_Q}{C_E}} \equiv v_F/g \tag{1.1}$$

$$Z_C = \sqrt{\frac{L_K}{4C_E} + \frac{L_K}{16C_Q}} \equiv \frac{1}{4g} \times \frac{h}{2e^2}\Omega = \frac{1}{4g} \times 12.9k\Omega \tag{1.2}$$

$$with\ L_K = \frac{h}{2e^2 v_F} \tag{1.3}$$

$$C_Q = \frac{2e^2}{hv_F} \tag{1.4}$$

With typical numerical values inserted [41], $v_P = 2.4 \times 10^8 cm/s, g = 0.33$ and $Z_C = 9.7k\Omega$. If g = 1, $v_P = v_F$, while for the many mode(classical)case, L_K and C_Q can be neglected and v_P=c, the speed of light in vacuum. Here, g is a factor that quantifies the strength of the electron-electron interaction in the SWCNT [42], [43]. These papers [42], [43] add *Maxwell's Equations* for the fields outside the CNTs, and claim they have a more accurate model than the *Transmission Line Model* of Burke [41]. In their model, the propagation velocity is different which changes the plasmon resonant frequencies, and when the CNTs are bundled, this further changes the propagation velocity.

C_Q was recently measured for a semiconducting SWNT and found to agree with the Lüttinger liquid theory [44]. The kinetic inductance for the semiconducting SWNT case was recently estimated based on direct microwave measurements [45]. Similar measurements have also been done on individual and bundles of metallic single-walled carbon nanotubes [46](see Figure 1.5). The Lüttinger liquid theory

predicts that the DC conductance has a power-law dependence on temperature and voltage, and this feature has been verified for metallic SWNTs in a number of instances [47], [48].

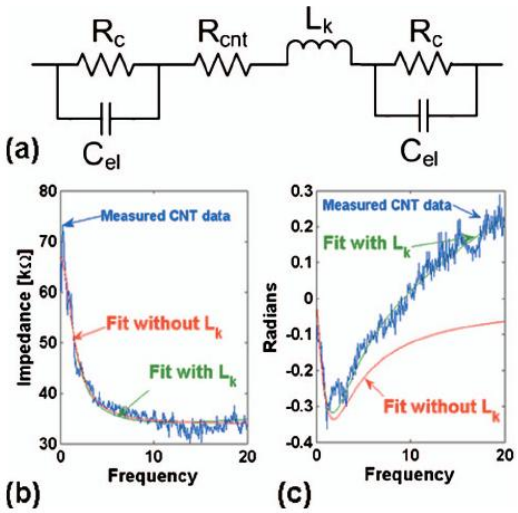

Figure 1.5. (a)Proposed circuit model for the SWCNT. (b)Results of fitting the circuit model to the measured CNT impedance data as a function of frequency with and without L_K. (c)Result of fitting the circuit model to the measured CNT phase angle data as a function of frequency with and without L_K, Ref.[46]

Given the above survey of metallic SWNT physics we can now predict the "Fabry-Perot" resonance frequency (lowest order mode) of a metallic SWNT with length L $= 1.0\mu m$:

$$f_r = \frac{v_P}{2L} = 1.2\ THz \tag{1.5}$$

1.2.2 Theory of high frequency detectors

In this thesis, we investigate the detection of microwave and terahertz radiation in m-SWCNTs. The m-SWNTs are predicted to potentially operate as detectors in one of two modes:(A)The bolometer mode: for this mode, the IF bandwidth in heterodyne operation is estimated as large as several hundred GHz [49]. (B)The diode mode: The SWNT detector will operate as a standard microwave detector and terahertz currents will be excited in the device that follow its I-V curve [50].

1.2.2.1 The diode mode

In this mode, the m-SWNTs will operate as a standard microwave detector and terahertz currents will be excited in the device that follows its dc I-V curves. We call the average DC voltage V_0, and the microwave voltage $\delta V = V_{RF} sin\omega t$. The I(V) function of the device can be expanded in a Taylor-series around the bias voltage V $= V_0$:

$$I(V_0 + \delta V) = \underbrace{I(V_0)}_{I_1} + \underbrace{\frac{dI}{dV}\delta V}_{I_2} + \underbrace{\frac{1}{2}\frac{d^2I}{dV^2}(\delta V)^2}_{I_3} + \cdots \tag{1.6}$$

The first three terms in the expansion can be identified as:

I_1 — The bias current.

I_2 — A sinusoidal component varying at the frequency ω. $\frac{dI}{dV} = R_B$ is the dynamic conductance.

I_3 — $\frac{1}{2}\frac{d^2I}{dV^2}(V_{RF} sin\omega t)^2$, the most important nonlinear term.

If the microwave amplitude is sufficiently small, then we can neglect any higher-order terms in the expansion. The time-average of the third term in (1.6) represents a small change in the DC current, which is proportional to the microwave power, and can be used to "detect" the microwave signal [50]:

$$< I_3 >= \frac{1}{2} \times \frac{d^2I}{dV^2} \times V_{RF}^2 \times \frac{1}{2} \tag{1.7}$$

note that:

$$< I_3 > \propto \ V_{RF}^2 \propto P_{RF} \tag{1.8}$$

A detector in this mode is often called a "square-law" detector because the output current is proportional to the square of the input voltage. The current sensitivity of

the diode detector is defined as the ratio of the output current into a short-circuit load, to the input power, i.e,

$$S_I \equiv \frac{I_{SC}}{P_{RF}} \tag{1.9}$$

$$S_V \equiv \frac{\delta V_{DC}}{P_{RF}} = S_I * R_B \tag{1.10}$$

Also, a similar derivation can be made for a heterodyne detector in the diode mode.

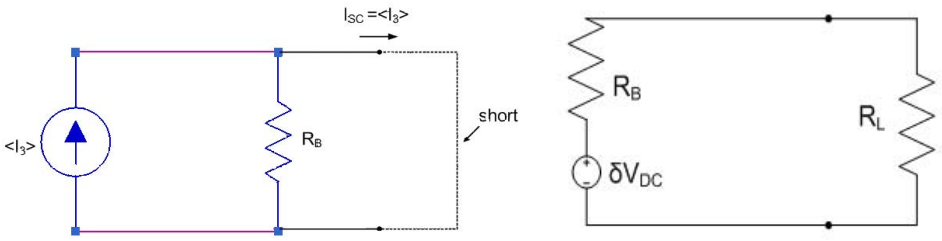

Figure 1.6. Alternative dc equivalent circuits of a microwave detector device, Ref[50].

1.2.2.2 The bolometer mode

The bolometer is a dissipative device that undergoes changes of resistance as changes in dissipated power occur. The nonlinear mechanism behind the bolometer is substantially different from that of Schottky barrier diode. In the latter, the currents at the millimeter wave signal(RF) frequencies basically follow the I-V curve, which can be measured at DC. The bolometer device, on the other hand, responds to the power at the RF frequency, not to the instantaneous voltage. This power heats the electron gas and/or the entire CNT medium, and as a result the resistance of the device changes. If only the electrons are heated to an electron temperature above the lattice temperature, then the device is called a "hot electron bolometer"(HEB). The change in resistance with electron temperature can come about because of a change in electron mobility, or electron density if it occurs, or a combination of these.

In the bolometer case as well, the responsivity of the detector can be predicted from the IV-curve. This theory has been verified for HEB detectors that utilize the 2DEG (2-dimentional electron gas) medium [51]–[53] and superconducting film devices [54]. An expression suitable for the CNT detector is [53]:

$$S_V = \frac{T_0 I_0 C_0}{1 - C_0 I^2} \tag{1.11}$$

Here, I_0=bias current.

T_0=mismatch loss factor.

$C_0 = \frac{R}{P} \cdot \frac{Z-R}{Z+R}$, which can be found from the IV curve, R=$\frac{V}{I}$ and Z=$\frac{dV}{dI}$ at the operating point. P=VI, the dissipated power at the operating point. Again, a similar derivation can be made for a heterodyne detector in the bolometer mode. The expression for C_0 inserted in (1.11) makes it clear that we are looking for nonlinear IV-curves ($Z \neq R$) in ordder to maximize S_V, just as was discussed for the diode mode. Heterodyne bolometer detectors are usually of the HEB type. An equivalent method for deriving S_v results in:

$$S_V = \frac{\Delta V}{P_{THz}} = \frac{I_0 \times R \times b}{[G_{th} + \imath\omega C]} (V/W) \tag{1.12}$$

Here, I_0 is the bias current, $b \equiv \frac{1}{R}\frac{dR}{dT}$, G_{th} is the thermal conductance from the device to the heat bath and C the heat capacity [51], [52], [55], see Figure 1.8. The thermal time-constant of the bolometer is $\tau_{th} = \frac{C}{G_{th}}$.

1.2.2.3 Photon-assisted Tunneling

Kim, et al. has done microwave detection on individual multiwall carbon nanotubes (MWNT) [56] and they claimed that the microwave power dependence of the linear conductance can be explained in terms of the photon-assisted transport.

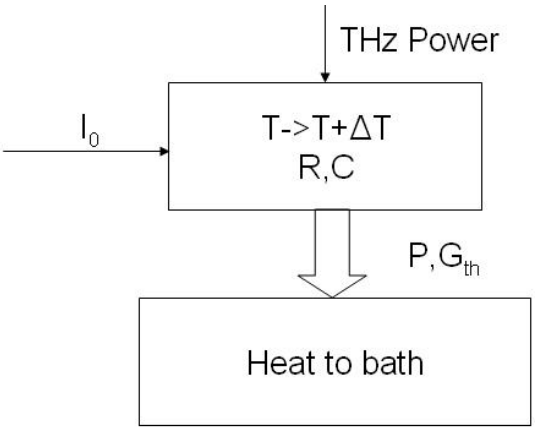

Figure 1.7. The heat flow diagram of the bolometer.

1.2.3 Possible application of SWCNTs as terahertz and microwave detectors

An m-SWCNT detector working in the diode mode has been demonstrated in our research group at microwave frequencies [47]. Several other experiments have also demonstrated microwave detection in semi-conducting SWCNTs (s-SWCNTs) fabricated as FETs with an additional gate electrode: (i) Rosenblatt et al [57] showed detection independent of frequency to about 10 GHz, with a one-pole roll-off measured to 50 GHz; (ii) Pesetski et al [58] measured heterodyne detection with a 10 KHz intermediate frequency. The response was flat when varying the RF and LO frequencies up to 23 GHz (see Figure 1.8); (iii) Rabieirad and Mohammadi also measured mixing, but at lower frequencies; (iv) Tarasov et al detected microwaves up to 110 GHz in bundles of SWCNTs at 4 K [59]. This reference did not make it clear whether m-SWCNTs or s-SWCNTs were involved; (v) Itkis et al demonstrated bolometric infrared photoresponse of suspended SWCNT films [60] see Figure 1.9, which is also related to the work in this thesis. In that case, G_{th} is very low since it is a suspended film, C, the heat capacitance, is very large, and τ_{th} is very long (milliseconds). (vi) Recently, two groups have demonstrated carbon radios based on different mechanisms: Rutherglen and Burke reported experimental results for a carbon nanotube (CNT) based amplitude-

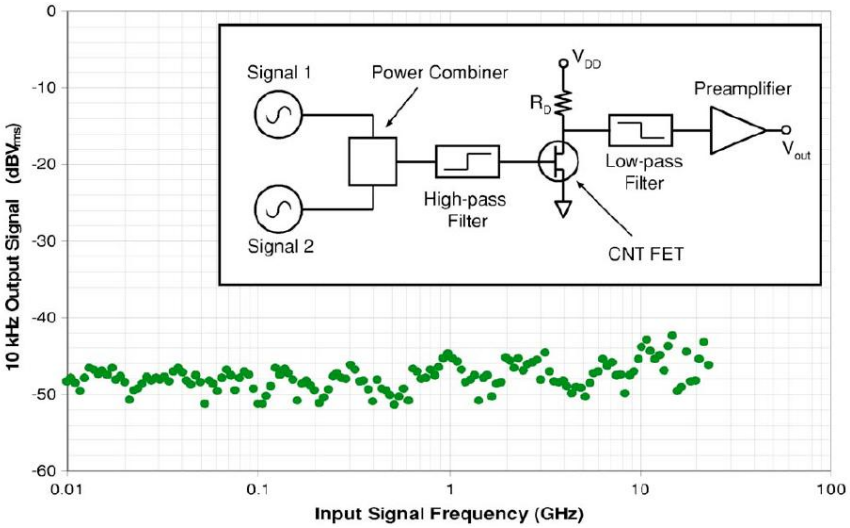

Figure 1.8. Experimental verification of FET operation at frequencies up to 23 GHz. The carbon nanotube FET amplifier is operated with an input signal containing two tones, at frequencies f and f +10 kHz. The FET acts like a mixer, producing an intermodulation product at 10 kHz. The amplitude of the 10 kHz output signal is plotted as a function of input frequency. We see no evidence of a rolloff caused by the CNT FET, even at 23 GHz, Ref[58].

modulated (AM) demodulator for modulation frequencies up to 100 kHz [61]. Jensen et al demonstrated a fully functional, fully integrated radio receiver from a single carbon nanotube. In that work, the mechanical properties of the carbon nanotube were employed [62]. Based on the above evidences, a very fast terahertz/microwave

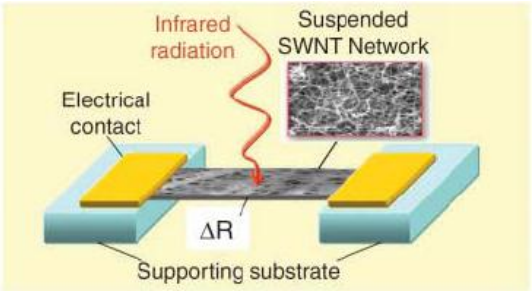

Figure 1.9. Diagram of SWNT network suspended between electrical contacts, Ref[60].

detector can be made employing SWNTs. In order to couple the terahertz photons to the carbon nanotubes, a quasi-optical coupling method can be used [63]–[65]. Note

that a semiconducting SWNT would require a gate electrode, which is difficult to realize in a terahertz detection configuration. Thus, in this thesis, metallic SWNTs are chosen for the experiments.

Comparison between different types of microwave and terahertz detectors is given in Table 1.1.

Table 1.1. Comparison between different high-frequency detectors

Detector	Frequency	Responsivity (V/W)	NEP[a] $Watts/\sqrt{Hz}$
Tunnel diode	10GHz	1000	–
Schottky diode	40GHz	5000	10^{-12}
Pyroelectric	THz	3000-10,000	10^{-9}
Semiconductor bolometer	THz	$10^3 - 10^4$	10^{-13}

[a]Noise equivalent power, the incident signal power required to obtain a signal equal to the noise in a one Hz bandwidth .

1.3 Scope of this Work

This thesis experimentally demonstrates terahertz detection in carbon nanotubes,and proposes models for these two different detection processes. This is done with a number of measurements, including direct detection measurements at several frequencies, power sweep and dc bias voltage sweep, and dc measurements at different temperatures.

The presently available terahertz sources becomes a major limitation in terahertz (THz) experiments, but we had access to two gas lasers with typical power of 1-10 mW. In this thesis, terahertz radiation between 0.69 THz to 2.54 THz is detected in single-walled carbon nanotubes. This is the first detection in a CNT to be reported for terahertz frequencies. These detections were done mainly at three different temperatures: ∼290 K(room temperature), 77 K(liquid nitrogen), and 4.2 K(liquid helium). Based on the experimental results, a bolometer model is proposed to explain

the detection process. For microwave detection, the difficulties lie in the large mismatch between the microwave test equiment(network analyzer,microwave probe,etc) and the device, which is the carbon nanotube bundle(s). This mismatch will cause large uncertainties in the post-processing results [66]. In this thesis, microwave signals up to 20 GHz are employed to measure the radio-frequency characterization of the device. The microwave data also help us to define the model for the CNTs at terahertz frequencies.

1.4 Organization of the Thesis

The thesis consist of four chapters outlined as follows. Experimental setup and results related to the carbon nanotube dc-characteristics and terahertz and microwave detection results are presented and analyzed in Chapter 2. Chapter 3 addresses fundamental explanations of the physical process for the detection. The bolometer model for the terahertz detection is proposed, and extracted element values for the circuit model of carbon nanotubes are also given. Possible future work are proposed in Chapter 4.

CHAPTER 2

EXPERIMENTS

2.1 Terahertz Measurements

The term *terahertz* (THz) was first used in the literature in the 1970's to describe electromagnetic (EM) waves with frequencies greater than 10^{12} Hz [67], [68]. Presently, this term is widely used when referring to frequencies from 300 GHz to 3 THz. (or equivalently free-space wavelengths from 1 mm to 100 μm) [1].

According to the Planck relationship[2], the quantum energy of terahertz photons ranges from 1.24eV to 12.4eV, which, as mentioned in section 1.2, corresponds to the band gap of quasi-metallic carbon nanotubes. Based on the *Transmission Line Model* (TLM) [41] of the carbon nanotubes, at THz frequencies, the contact resistances are bypassed due to the parallel contact capacitances, thus the intrinsic properties of the carbon nanotubes can be investigated.

2.1.1 Device Preparation and Configuration

In this thesis work, the measured carbon nanotubes were grown using the Chemical Vapor Deposition (CVD) method [69], [70]. The length of the tube is around 50 μm, the outer diameter is between 1 nm and 2 nm, and the purity of the single-walled carbon nanotubes is greater than 90 wt%. In addition to the CVD discharge method, there are several other methods to grow carbon nanotubes [71]–[75].

---

[1] This part of the electromagnetic spectrum is also commonly refered to as far-infrared (FIR) or submillimeter (sub-mm).

[2] $E = h\nu$, $h = 6.626068 \times 10^{-34} J \cdot s$ is Planck's constant, ν is the frequency of the electromagnetic wave.

The test structure on which the carbon nanotubes are integrated and tested in the THz measurements is a planar log-periodic antenna (LPA), shown in Figure 2.1. The LPA is one instance of self-complementary antennas, which have a constant input impedance, independent of the source frequency and of the shape of the structure [76]. This property makes it one of the best candidates in the THz frequency range. The size of the LPA is $200\,\mu m \times 200\,\mu m$, and the gap in the center is around $8\,\mu m$[1]. There is an array of the LPA structures on the chip, usually the center LPA of the array is used for the measurements. The chip size is $6\,mm \times 6\,mm$.

Figure 2.1. Microscope picture of a planar log-periodic antenna.

The substrate of the chip is made of either sapphire or silicon-on-sapphire (SOS), which show good transmission up to high THz frequencies (the band gap of silicon and sapphire is 1.12 eV and 9.9 eV respectively). The substrate has a thickness of $400\,\mu m$. The deposited metal of the LPA is gold with a thin layer of titanium (20 nm) for adhesion, and the total thickness of the metals is about 100 nm, see Figure 2.2.

[1]The shape of the gap is not perfectly rectangular but with some curvatures

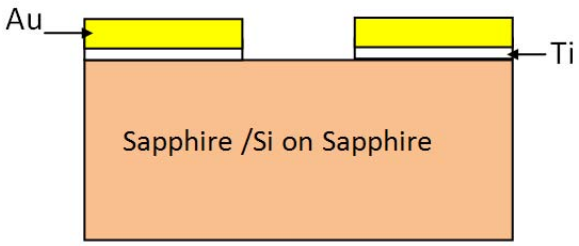

Figure 2.2. Diagram of the metal and semiconductor layers

The carbon nanotubes contacted to the center gap of the antenna are prepared with dielectrophoresis (DEP) process [77]–[79]. The diagram of the DEP process is shown in Figure. 2.3.

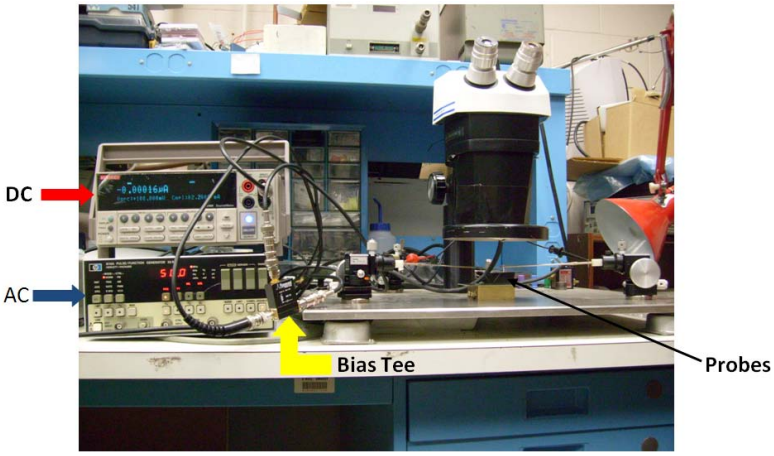

Figure 2.3. Diagram of the setup of the DEP process.

A drop of a suspension of CNTs in isopropyl alcohol (IPA) is applied in the contact area. The CNTs will then drift to the narrow gap in the contacts and attach to them. The ac signal, which is sinusoidal in this case, is supplied by a function generator. Its amplitude is 4 volts, and the frequency is 5 MHz[1]. A small dc voltage of 100 mV is also applied to monitor the changes of the resistance between the gap. Ac and dc signals are coupled through a bias tee. At the beginning of the DEP process, the measured resistance is infinite, then it will decrease, and the process is halted when the DC resistance is sufficiently low. The result is that a small number of bundles of CNTs

[1]In practice, different amplitudes and frequencies were tried for DEP.

will be contacted in parallel. The CNTs have large mutual van der Waals forces that make them form bundles. Breaking the bundles apart requires that one employs a surfactant which we did not do. The lower resistance of these devices compared with typical single SWNTs, from $5\,k\Omega$ to $50\,k\Omega$, facilitates matching of microwaves or THz radiation to the CNTs. The DEP process primarily acts on metallic CNTs. While semiconducting tubes are expected to be present in the bundles, we assume these to have a negligible effect (at DC) due their known higher resistance.

After getting a proper[1] I-V curve, then an annealing process is needed. It is done by heating the chip in an oven to about 200°C for 45 minutes, then let it cool down. With the annealing process, usually we can get better contacts.

To efficiently gather the THz power to the gap of the LPA, where the carbon nanotubes will be located, an elliptical silicon lens with a diameter of 4 mm is mounted on the backside[2] of the chip with bees wax. This configuration has shown very efficient transmission and focusing of THz waves in traditional HEB detection devices [80]–[82]. A functional description of such a configuration is shown in Figure 2.5. In this work, there are three devices being tested, see Table 2.1.

Table 2.1. Devices tested in this thesis work

Device	Substrate	Resistance at room temperature	Resistance at low temperature	Antenna
A	SOS	$833\,k\Omega$	$870\,k\Omega$ (77K)	LPA
B1	Sapphire	$7\,k\Omega$	$11.5\,k\Omega$ (77K)	LPA
B2	Sapphire	$20.3\,k\Omega$	$31.7\,k\Omega$ (77K) $41.8\,k\Omega$ (4.2K)	LPA

The above configurations need to fit into a metal block, see Figure 2.6. The metal block has a circular hole in one side to let the silicon lens face the THz radiation. The block has one SMA[3] connector, the outside of the connector is connected to the

[1] We prefer a resistance of about several tens of $k\Omega$ and some kind of nonlinearities.

[2] Backside here is the side without metallization

[3] SMA stands for SubMiniature version A, a typical microwave connector.

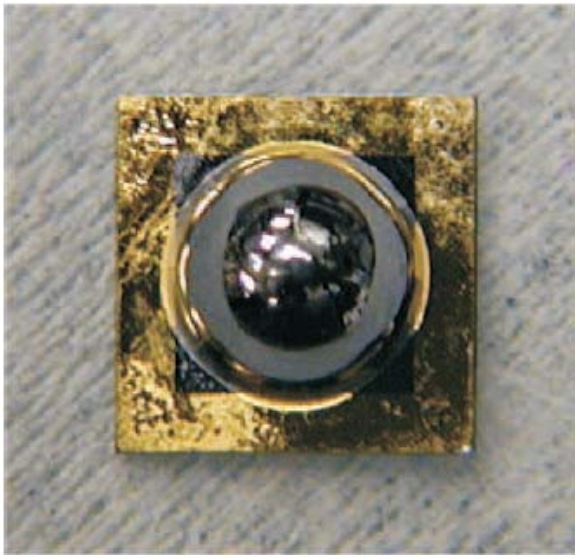

Figure 2.4. Photograph of the backside of the chip with the silicon lens.

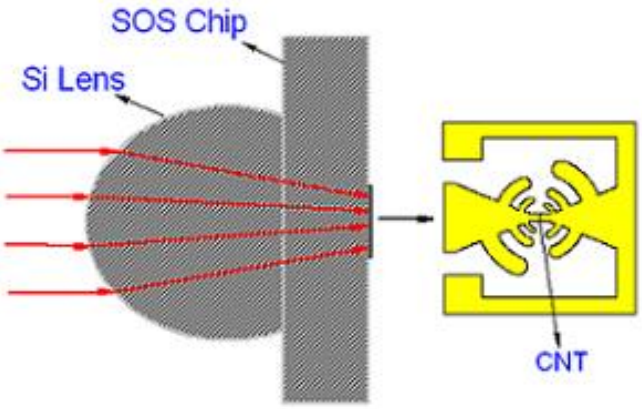

Figure 2.5. The functional description of the detection block.

ground, which is the walls of the metal block in this case, and the center conductor connected to a microstrip inside the metal block. The 'chip-lens' configuration is mounted into the metal block using epoxy. Then the two separate branches of the LPA are bonded to the microstrip and ground using gold wires. The lengths of the two gold wires are about 5 mm and 8 mm, see Figure 2.4. Now the block is ready

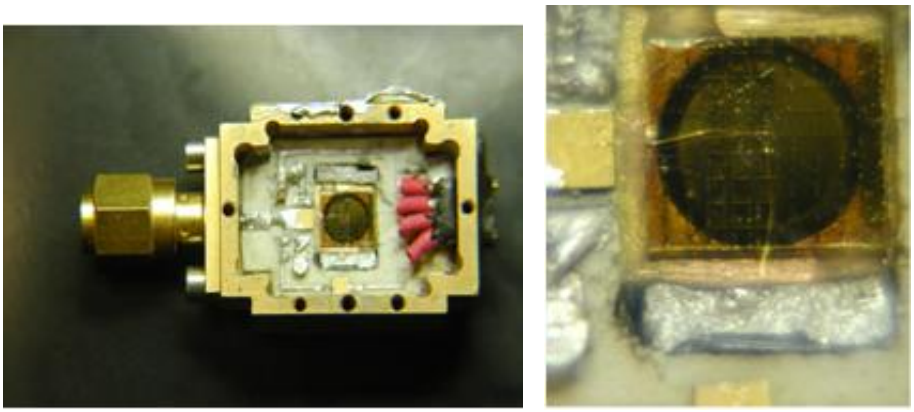

Figure 2.6. The detection block and the wire bonded chip.

to install into the liquid helium (LHe) cryostat (dewar). Our cryostat belongs to the HDL-5 series manufactured by Infrared Labs Inc., Tucson, AZ (Figure 2.7). The dewar has an outer radiation shield that is cooled to 77 K and a 1.2 liter liquid helium can to maintain the DUTs (Device under test) at their nominal temperature. A high density polyethylene (HDPE) window is used at 300 K to provide good THz transmission while withstanding the pressure difference while the dewar is under vacuum. Zitex is used as the IR filter on the 77 K radiation shield. With a good vacuum, hold times of 10 hrs can be achieved under typical thermal loading [80].

2.1.2 Experimental Setups

The diagram of the experimental setup is shown in Figure 2.8. The incident EM wave is the output of an FIR laser optically pumped by a CO_2 laser. The CO_2 laser is modulated by a square wave from the function generator via an acoustic-optic modulator (AOM). The typical modulation frequency, which will not bring significant

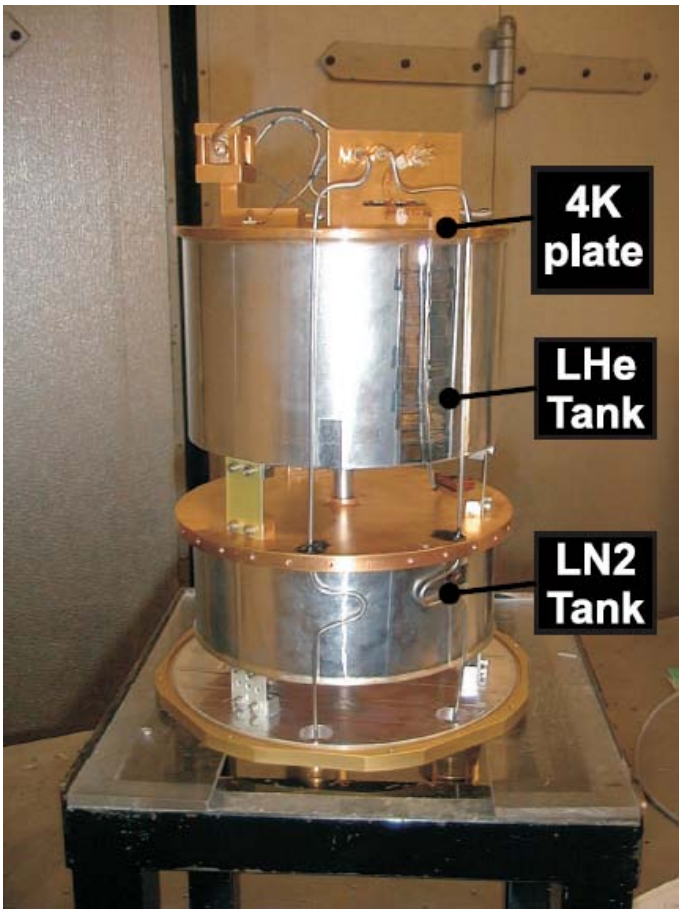

Figure 2.7. Photograph of the liquid helium dewar.

amplitude or phase effects, is up to 2 KHz. In these measurements, the modulation is set to 1 KHz. The DC supply and measurements are fulfilled with a Keithley voltage source and a four-wire measurement fixture. A 100 $k\Omega$ resistor is connected in series with the carbon nanotube, and the dc supply is connected directly to the resistor. The voltage across the two terminals of the carbon nanotubes is measured by the Vsense port[1]. The Keithley also measures the current through the carbon nanotubes.The detected signal is measured with a Lock-In amplifier (EG&G 7260 DSP Lock-In Amplifier), which has an input impedance of 1 $M\Omega$, and uses the signal from the function generator as reference.

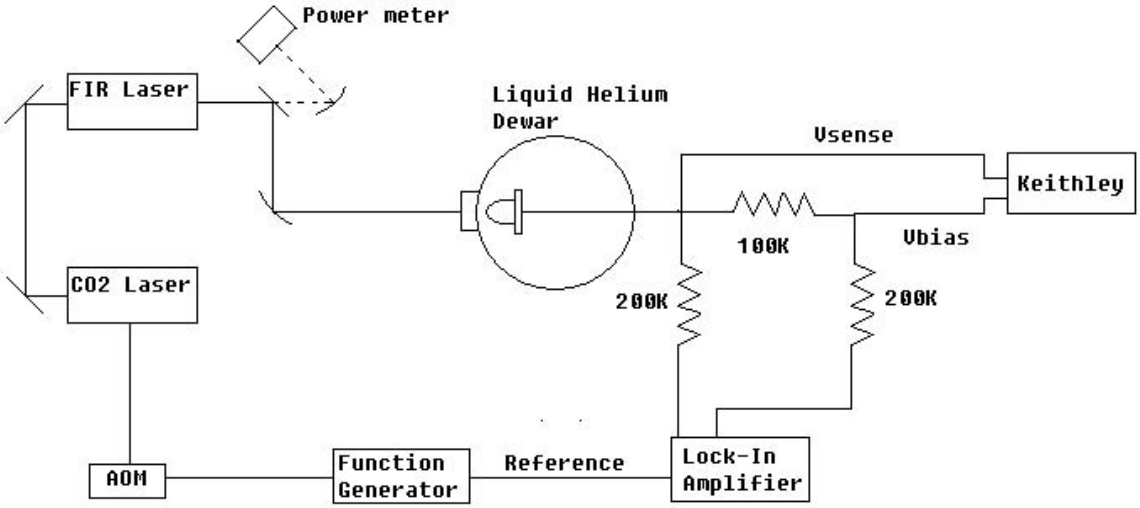

Figure 2.8. The diagram of the experimental setup.

2.1.2.1 Terahertz source

The terahertz source used in this work is a CO_2 laser pumped far-infrared (FIR) gaseous laser. Although solid state sources with sufficiently high power have become recently available [83]–[85], an FIR laser system is very well-suited for extensive laboratory testing. Our system produces stable continuous-wave (CW) THz radiation with an output power up to about 100 mW for the strongest lines. The THz laser

[1]In some experiments with lower resistance CNTs the current sensing resistor has a lower value.

can be readily tuned to different frequencies by changing the gas in the FIR tube. The laser lines used during the experiments presented in this thesis are summarized in Table 2.2.

Table 2.2. Summary of common laser lines used in this investigation.

Wavelength [μm]	Frequency [THz]	Pump line	Medium	FIR power [mW]	Pressure [mTorr]
432	0.694	9R20	Formic acid	5	80
287	1.05	9R34	Difloromethane	5	90
215	1.39	9R34	Difloromethane	5	80
184	1.63	9R32	Difloromethane	10	100
118	2.54	9R36	Methanol	15	90

Figure 2.9. Photograph of the CO_2-pumped far infrared (FIR) laser used as THz source.

2.1.2.2 DC biasing

The device under test (DUT) generally needs a dc voltage bias, so we can investigate the detection responsivity versus bias voltage to understand the detection process of the carbon nanotubes. The I-V curve, which is a fundamental property of a device, can be examined as well. The biasing scheme used with our CNT-LPA

structures is a 4 - wire biasing system, which is based on the same topology used with the HEB mixers in our group [80]. However, instead of using a external feedback control box, we are using the Keithley sourcemeter which has a 4-wire sense function and a external 4-wire fixture.

2.1.2.3 Temperature sensor

In this investigation, dc and terahertz measurements at different temperatures are very important, since the behaviors of carbon nanotubes as a function of temperature give a lot of insights into the carbon nanotube detection processes. Detailed discussion of the detection model of the carbon nanotubes will be made in Chapter 3. Thus an accurate measure of the temperature of the device is necessary. In this work, it is realized by using a silicon diode temperature sensor, which has a temperature dependent bandgap voltage. The sensor is mounted using a screw onto the cap of the block with a thin layer of Indium in between.

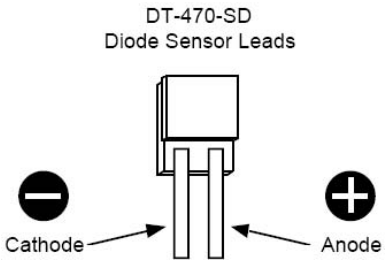

Figure 2.10. Diagram of the silicon diode temperature sensor.

2.1.3 Results

2.1.3.1 DC results

The I-V curves of three different devices (A, B1, B2) at different temperatures were measured. The differential conductances (dI/dV) of these curves are also calculated (Figure 2.11–2.13, red curves on the right scale).

All of these I-V curves show a concave up shape, that is due to the Ti/Au contact. Furthermore, the first-order derivatives show a 'zero-bias anomaly' (ZBA) [86], i.e. the

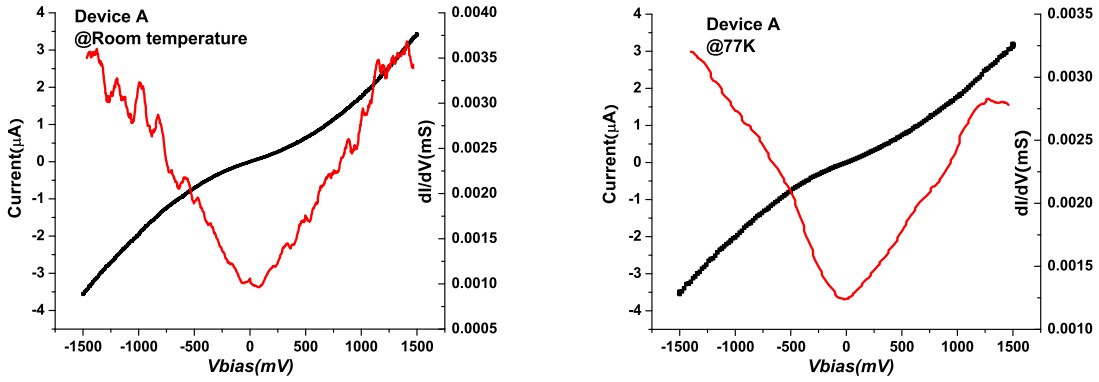

Figure 2.11. I-V curve of device A at room temperature (left) and at 77 K (right).

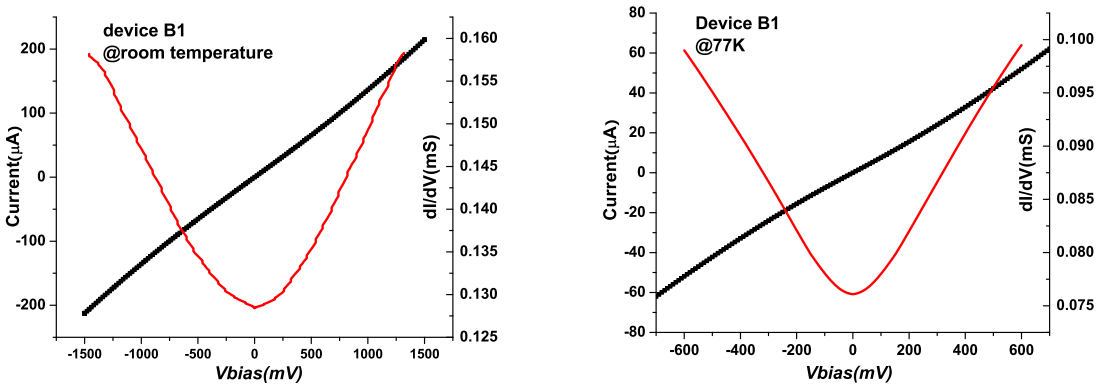

Figure 2.12. I-V curve of device B1 at room temperature (left) and at 77 K (right).

differential conductance plotted as a function of bias voltage (Vbias) shows a dip at low values of Vbias. This presents a nonlinearity in the I-V curves that we exploited for both microwave and terahertz detection detection.

2.1.3.2 Terahertz detection results

Terahertz detection was performed at several different THz lines and different temperatures. The typical temperatures used in this investigation are 300 K (room temperature), 77 K (liquid nitrogen) and 4.23 K (liquid helium). The bias voltage dependence of the detector response to terahertz radiation does not have a simple

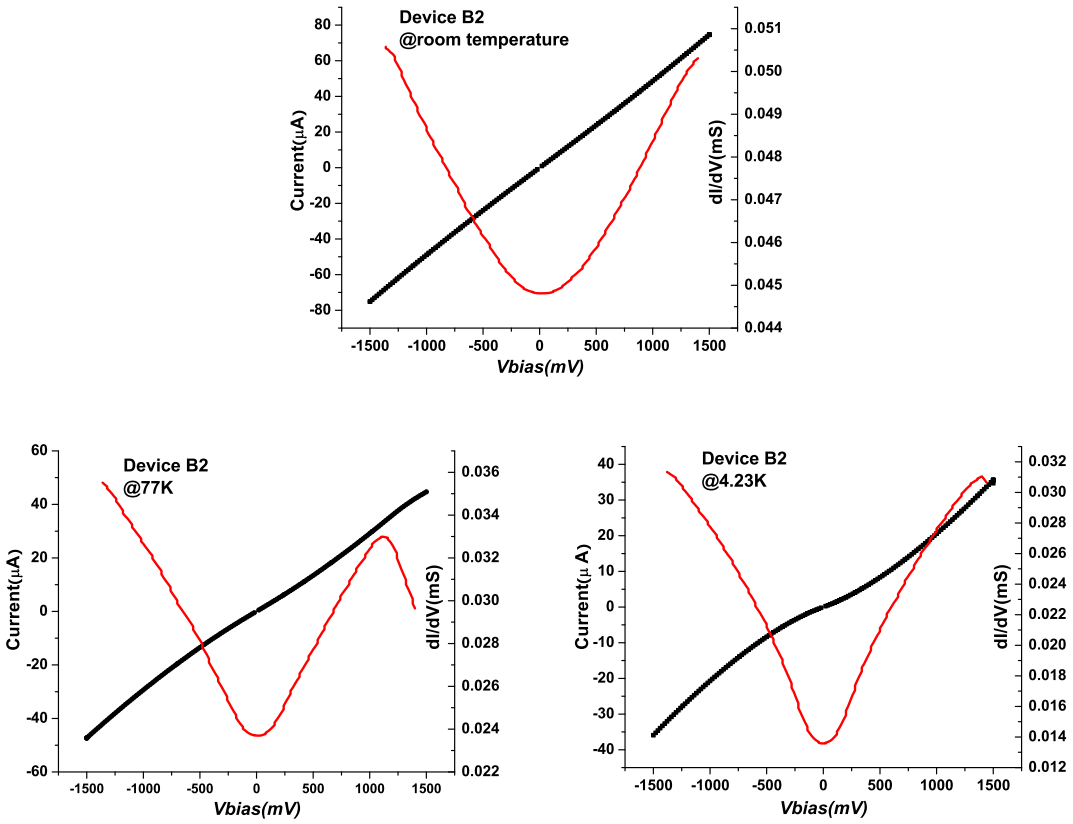

Figure 2.13. I-V curve of device B2 at room temperature (upper left), 77 K (upper right) and 4.23 K (bottom).

d^2I/dV^2 dependence. This makes it clear that we need to search for a different detection process at THz compared with GHz, as will be discussed further in Chapter 3. The detected voltage was also measured with the input terahertz power varied by a grid attenuator. The results shows that all of our measurements lie in the linear region of S_V as a function of laser power.

In Figure 2.14(b), the four sharp peaks in the magnitude of the response (at about 700 mV and 1,050 mV, resp., and at - 50 mV and -300 mV) are reproducible. We have never figured out what they are due to; device B did not show them, so they may occur primarily in high contact resistance devices. We also detected frequencies

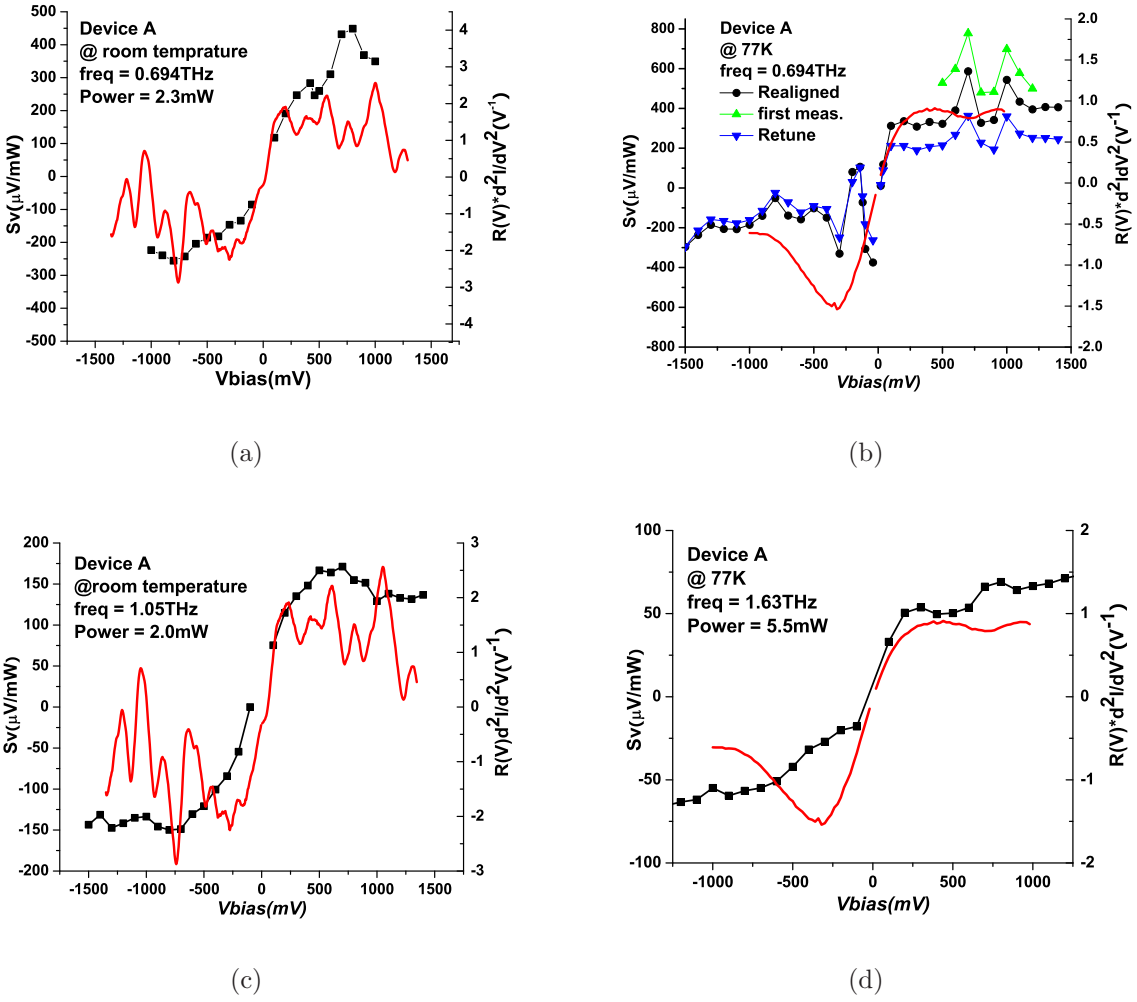

Figure 2.14. Terahertz detection results for device A(black dots, left scale) and comparison with results from diode model(red curves, right scale).

1.05 THz and 1.63 THz, but did not see the sharp peaks in Figure 2.14(c),(d) at these frequencies.

Device B1 (like Device A) shows detection at 694 GHz and 300 K, see Figure 2.15(a), the input terahertz power is 1.75 mW. However, S_V was only 0.2 V/W. At 77 K, S_V was 9.2 V/W at 694 GHz and 0.7 V/W at 1.05 THz, the input terahertz power was 1.1 mW and 2.05 mW, respectively at these two frequencies.

Device B2 shows detection at 300K, 77K and 4.23K, see Figure 2.16. At 300K, the responsivity is only 0.022 mV/mW at 1.4 THz; at 77K, Sv is from 0.412 mV/mW to 2.32 mV/mW at 2.54 THz and 1.4 THz; at 4.23K, Sv are much higher, from 3.8 mV/mW to 10.5 mV/mW. The summary of the terahertz detection responsivities of these devices is shown in Figure 2.17.

2.1.3.3 Results of measurements regarding temperature dependence

With the temperature sensor, the dc and terahertz detection measurements can also be taken as a function of the temperature. In this investigation, the temperature sensor was only installed on the block with device B2. The I-V curves are shown in Figure 2.18. The non-linearity of the curves decreases when temperature increases from 4.23K to 300K.

At 694 GHz and a dc bias voltage of -1500 mV, the detected voltages on the lock-in amplifier were recorded at different temperatures as the temperature increased from liquid helium (4.23 K) to about 180 K, see Figure 2.19. Above 160 K, the signal was not detectable.

From the I-V curves at different temperatures, the resistances at different temperatures and dc bias voltages can be derived, see Figure 2.20.

In the log scale plot (bottom in Figure 2.20), at a certain range of temperatures, between 10 K and 100 K, the relation between the resistance (R) and the temperature (T) is quite linear, this indicates that the resistance is a power function of the

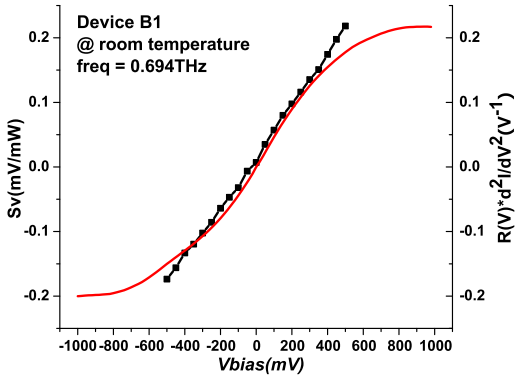

(a) Responsivity of terahertz detection of Device B1 at 0.694 THz and 300 K.

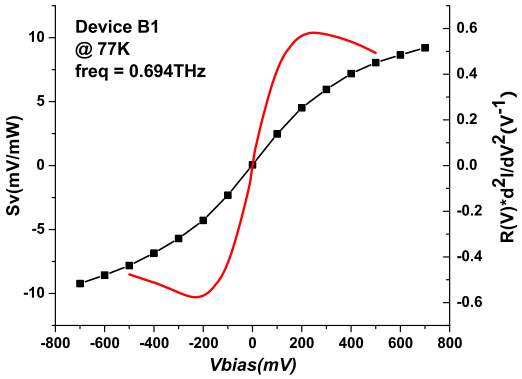

(b) Responsivity of terahertz detection of Device B1 at 0.694 THz and 77 K.

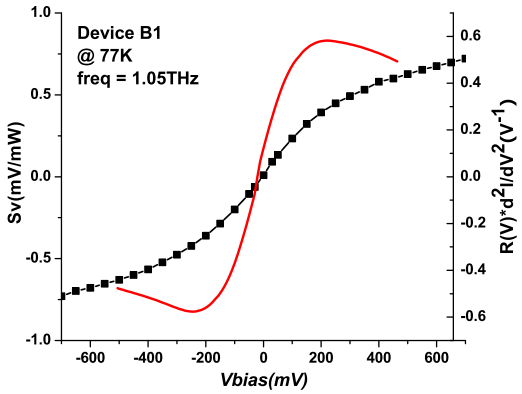

(c) Responsivity of terahertz detection of Device B1 at 1.05 THz and 77 K.

Figure 2.15. Responsivities of terahertz detection of Device B1(black dots, left scale) and comparison with diode mode data(red curves, right scale).

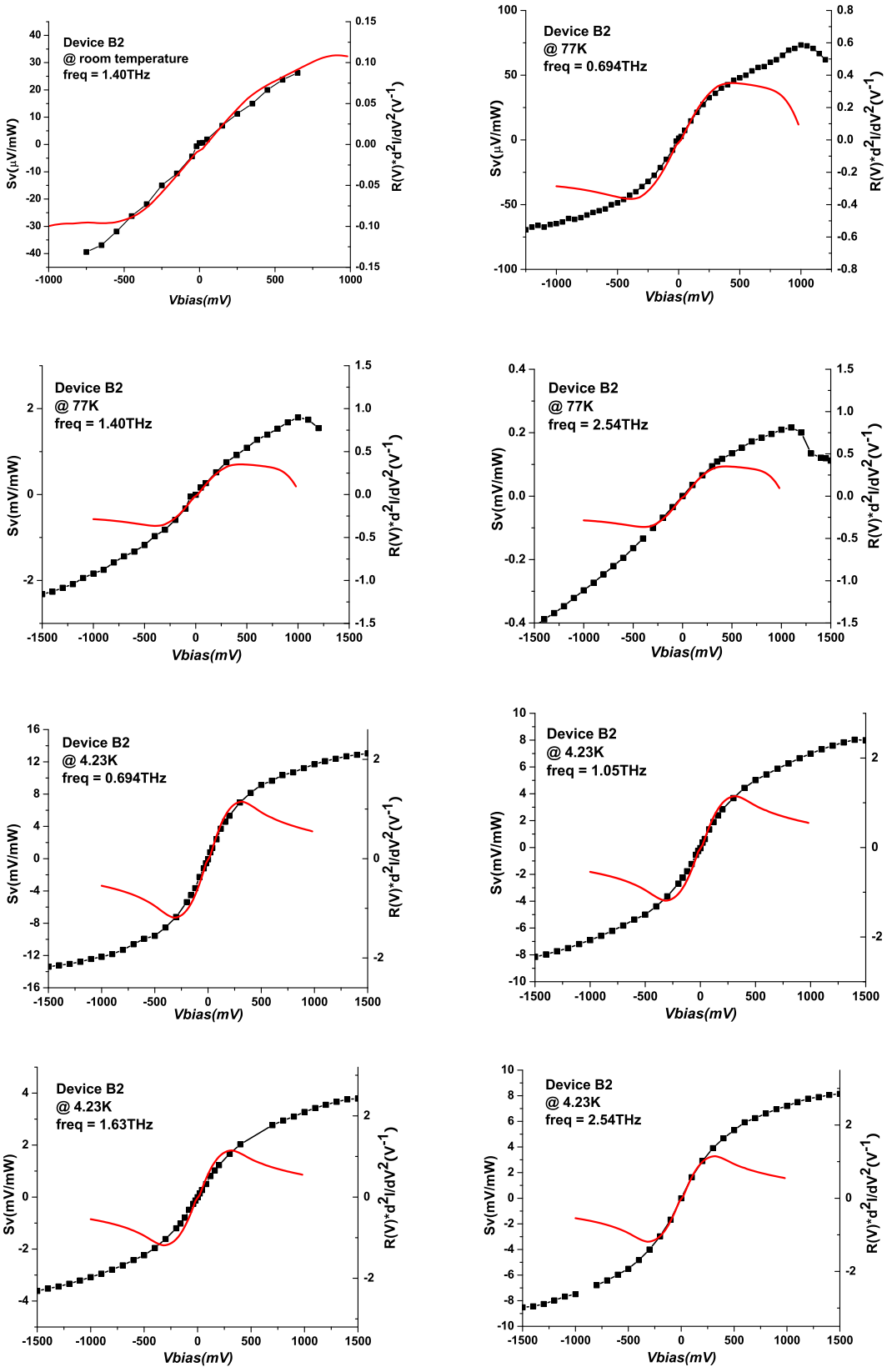

Figure 2.16. Responsivities of terahertz detection of Device B2(black dots, left scale)compared with the diode mode data(red curves, right scale).

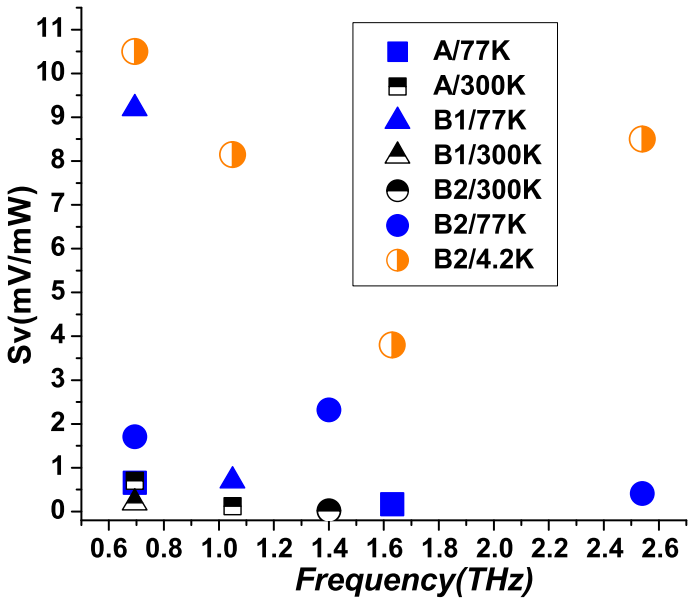

Figure 2.17. Summaries of the responsivities of the terahertz detection.

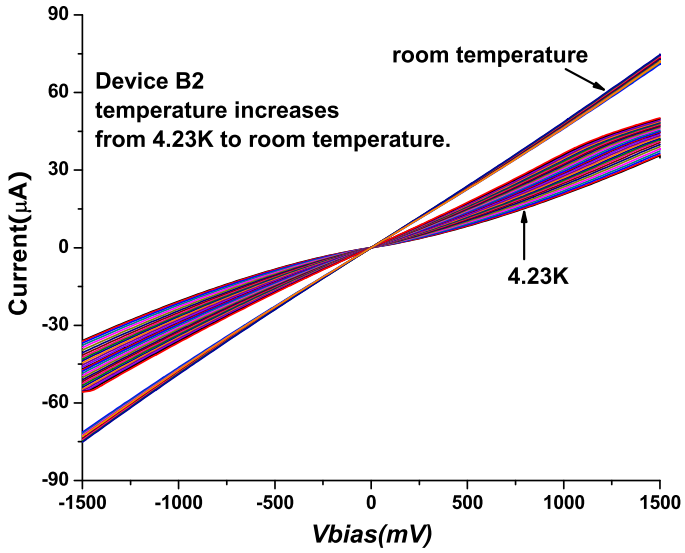

Figure 2.18. I-V curve of device B2 at different temperatures.

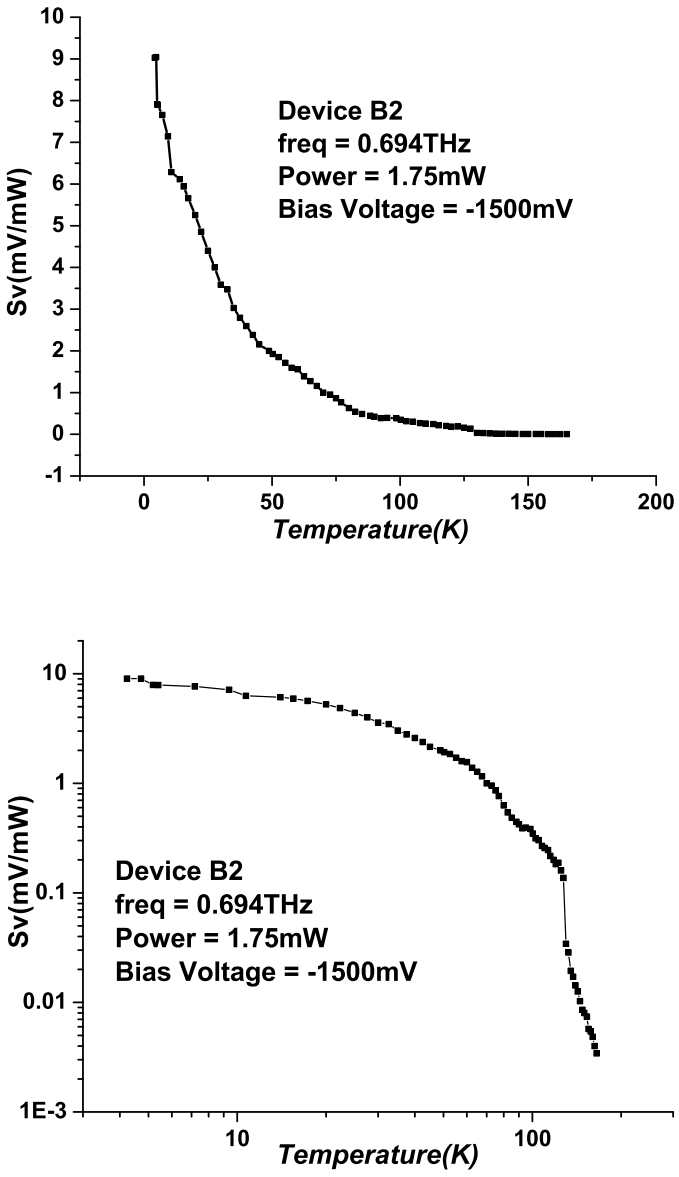

Figure 2.19. Terahertz detection on device B2 as a function of the temperature both in linear scale (left) and log scale (right).

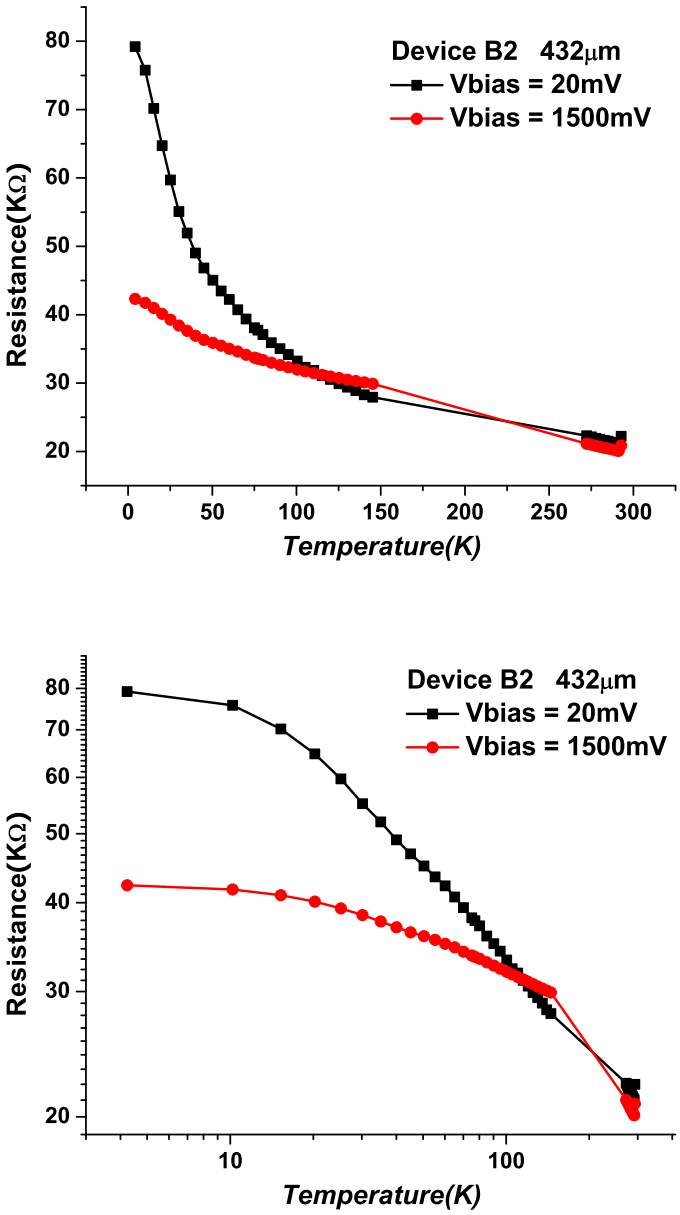

Figure 2.20. Resistances of device B2 as a function of the temperature both in linear scale (left) and log scale (right).

temperature, i.e. $R = \mathcal{C}T^{\alpha}$. When the dc bias voltage is 20 mV, the relation is $R = 196.2T^{-0.381}$, and when dc bias voltage is 1500 mV [87], the relation changes to $R = 59.64T^{-0.13}$, this is similar to the values in [87]. The approximate power-law behavior suggests that the nanotubes behave as a Lüttinger liquid (LL).

2.2 Microwave Measurements

Microwave measurements can also address the dynamic performance of CNTs. However, unlike terahertz radiation, there is no elliptical lens and antenna to couple the microwave signal to CNTs; the microwave signal is coupled to the CNTs directly through either the bond wires or microwave probes. One major impediment to applying high frequency signals to CNTs is that a high impedance exists at the metal/CNT interface [88].

2.2.1 Device configurations

In microwave measurements, the CNTs are also prepared with the DEP process. The devices are measured with two different configurations: one is using the same fixture used in the terahertz measurements; in which case a microwave signal is sent into the device through the SMA connector as well as the dc signal; the structure here is still the log-periodic antenna (LPA); the other configuration is the so-called CPW (co-planar waveguide) structure (Figure 2.21), which is widely used to transport microwave signals, and this structure is perfect for the microwave probe measurement. The devices used for microwave measurements are listed in Table 2.3[1].

2.2.2 Experimental Setups

In the microwave measurements, the experimental setups are similar to the terahertz detection (Figure 2.22), here, only the high frequency source and the way it

[1]Note that the substrate used in all these cases is SOS which yields much smaller parasitic capacitance than the heavily doped silicon substrate that was used earlier in our research group.

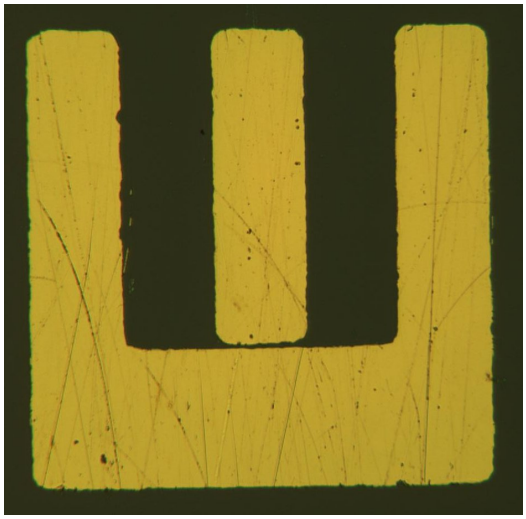

Figure 2.21. Photograph of the co-planar waveguide structure.

Table 2.3. Devices tested in the microwave measurements

Device Name	Substrate	Resistance at room temperature[a]	Antenna	Measured in
A	SOS	$833\,k\Omega$	LPA	Fixture
C	SOS	$4.1\,k\Omega$	CPW	Microwave probe
D	SOS	$10.5\,k\Omega$	CPW	Microwave probe
E1	SOS	$10.2\,k\Omega$	CPW	Microwave probe
E2	SOS	$85\,k\Omega$	CPW	Microwave probe
F	SOS	$7.5\,k\Omega$	LPA	Microwave probe

[a]at low bias voltage

couples to the CNTs change. Instead of a terahertz gas laser, an Agilent 8251A microwave signal generator is used as the ac source (0.1-20GHz). The dc bias system is the same as the one used in terahertz detection, the dc and ac signals are coupled to the device through a bias-tee (Picosecond 5541A). The detected low frequency (1KHz) signal was measured by the lock-in amplifier (AG&G 7260).

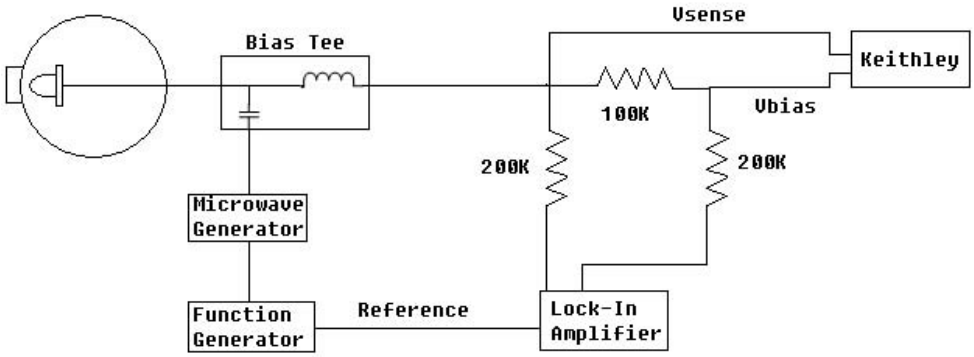

Figure 2.22. Diagram of the microwave measurement setups.

2.2.3 Results

For the microwave devices, dc measurements, detection measurements and the S-parameter measurements are presented here. With more functionalities of the microwave source, the frequency and the power can be easily adjusted, that makes continuous frequency and power sweep feasible.

2.2.3.1 DC results

The I-V curves and the differential conductances are shown in Figure 2.23. The red curves on the right scale are the differential conductances, dI/dV. Like the devices in terahertz measurements, these curve also show a zero-bias anomaly (ZBA).

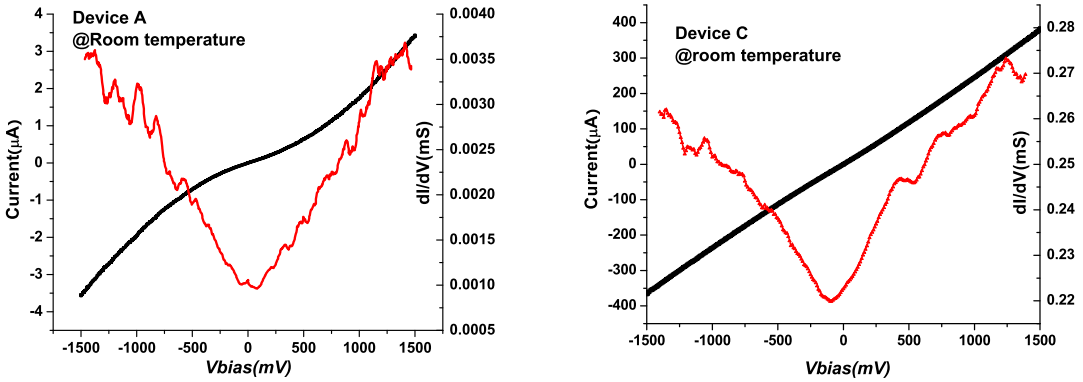

(a) I-V curve of device A at room temperature. (b) I-V curve of device C at room temperature.

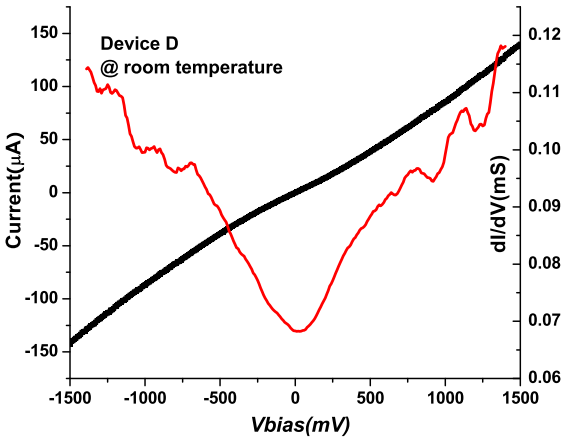

(c) I-V curve of device D at room temperature.

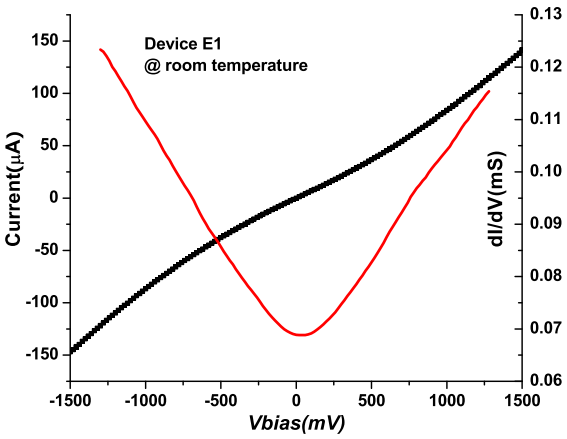

(d) I-V curve of device E1 at room temperature.

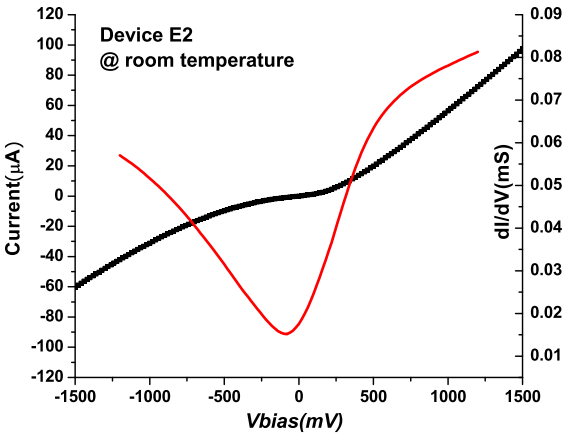

(e) I-V curve of device E2 at room temperature.

Figure 2.23. DC results of different devices.

2.2.3.2 Microwave detection

As mentioned above, microwave detection can be measured as a function of bias voltage, frequency and also power. The measurements in the fixture could be performed at cryogenic temperatures, but had the disadvantage that the fixture introduces much larger parasitics. The results of detection as a function of the dc bias voltage are shown in Figure 2.24. The variation of S_V with V_{bias} shows a general resemblance to $R \times \frac{d^2I}{dV^2}$ as expected from the diode model, see Equation (1.7) and (1.10). There are some extra sharp features, small peak shifts, etc. We expect that these are due to the complex structure of the devices prepared by DEP. On the contrary, single m-SWNTs as reported in [47] yield a much better agreement.

Notice that the power level of the microwave source is rolling off as frequency increases. So we measured both the detection voltage (vlock) and output power, i.e. the input power at the probe as a function of frequency, and then we normalized the frequency response of the CNTs, see Figure 2.25.

We measured the detection voltage as a function of the input power level of the probe in order to pick a power level at which the detection in still in the linear region. Only in the linear region, can we perform the normalization as above. Here, 'linear' means that the detection voltage is a linear function of the power level, but it is usually called 'square-law' since the detected voltage is proportional to the square of the input voltage (V_{in}^2), see Figure 2.26.

2.2.3.3 S-parameter measurement

For a one-port device, the S11 parameter is important in the sense that it gives the impedance of the device over a wide range of frequencies, so the circuit model using lumped elements of the device can be obtained. Thus the microwave detection can be simulated from that circuit model. S11 is defined as: $S11 = \frac{Z_{in} - Z_0}{Z_{in} + Z_0}$, so it can be easily converted to Z parameters or Y parameters. S11 was measured for CPWs

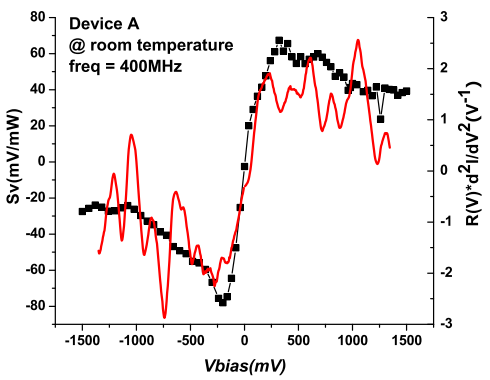

(a) Detection vs. bias voltage of device A .

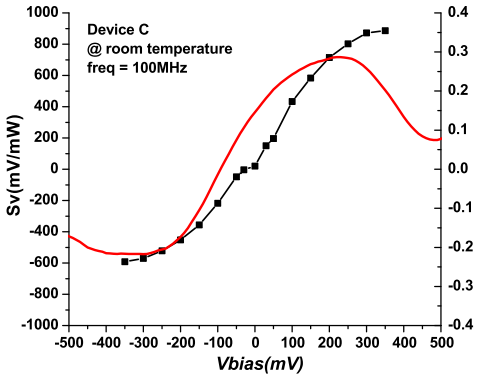

(b) Detection vs. bias voltage of device C.

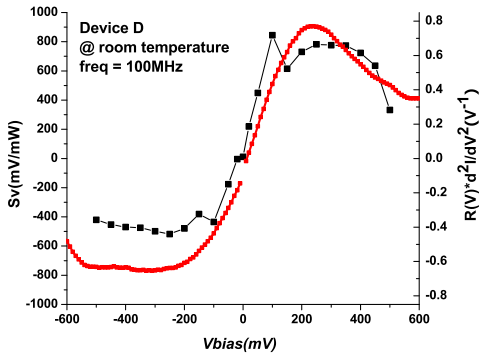

(c) Detection vs. bias voltage of device D.

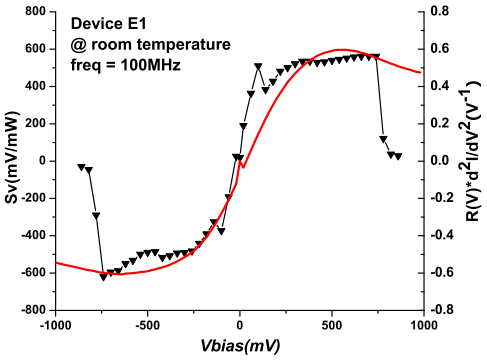

(d) Detection vs. bias voltage of device E1.

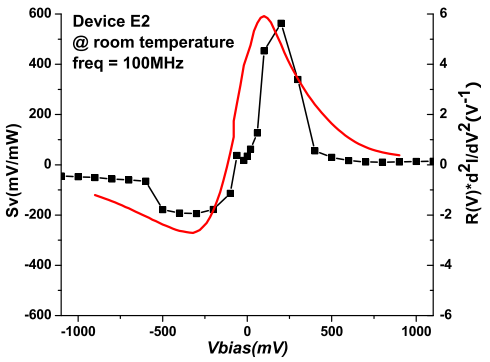

(e) Detection vs. bias voltage of device E2.

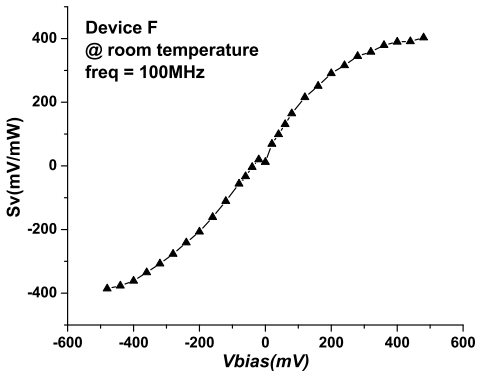

(f) Detection vs. bias voltage of device F.

Figure 2.24. Microwave detection as a function of bias voltage of different devices(black dots, left scale) and the diode mode data(red curves, right scale).

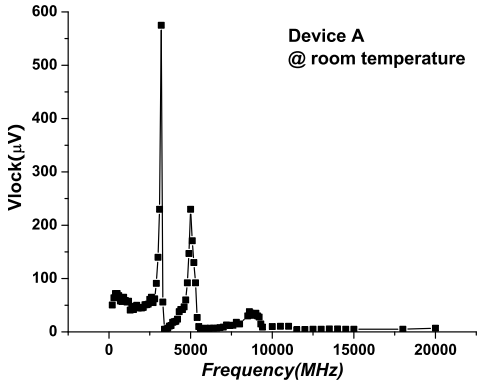

(a) Detection vs. frequency of device A at room temperature, measured in the fixture.

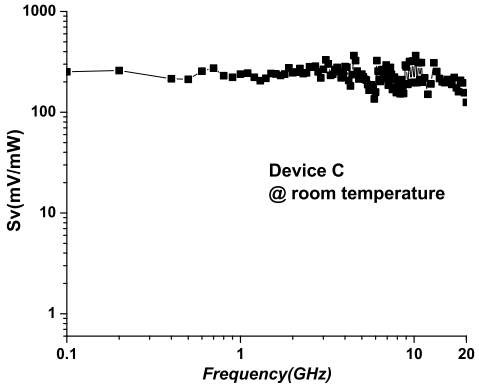

(b) Detection vs. frequency of device C at room temperature, (the following measurements were also all preformed with the microwave probe).

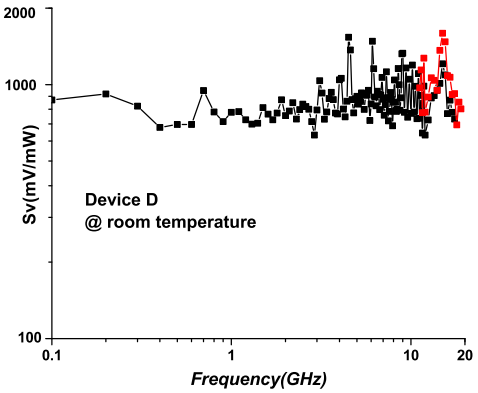

(c) Detection vs. frequency of device D at room temperature, the red curve is the second measurement.

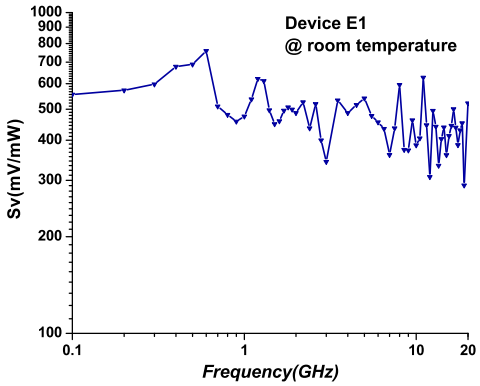

(d) Detection vs. frequency of device E1 at room temperature.

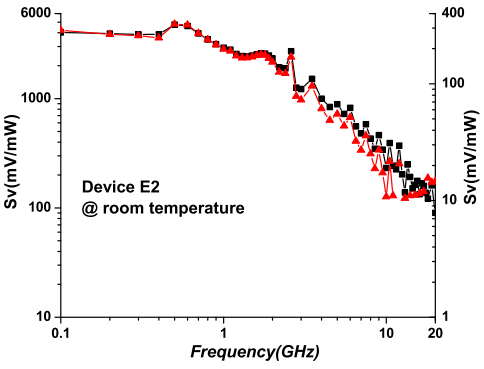

(e) Detection vs. frequency of device E2 at room temperature, red curve is a second measurement on the right scale.

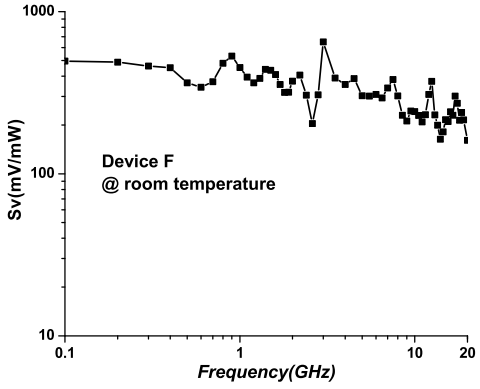

(f) Detection vs. frequency of device F at room temperature

Figure 2.25. Microwave detection as a function of microwave frequency of different devices.

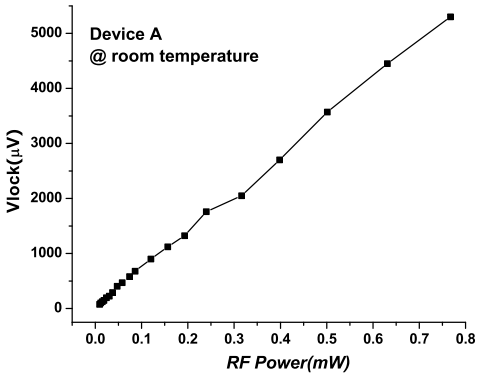

(a) Detection vs. microwave power level of device A at room temperature.

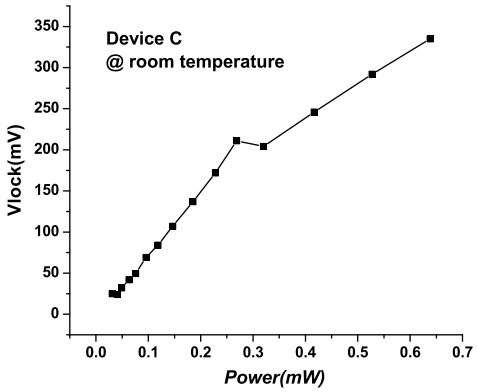

(b) Detection vs. microwave power level of device C at room temperature.

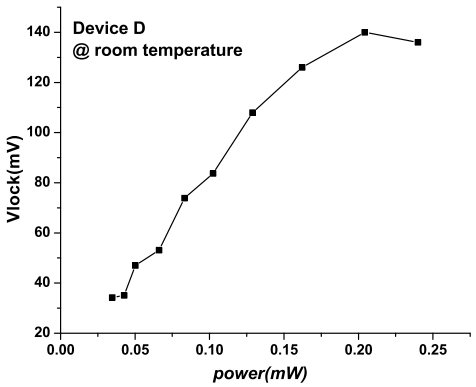

(c) Detection vs. microwave power level of device D at room temperature.

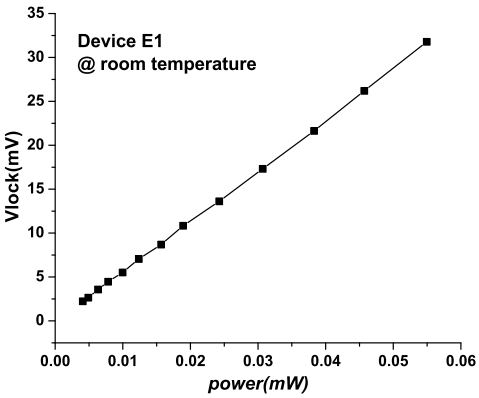

(d) Detection vs. microwave power level of device E1 at room temperature.

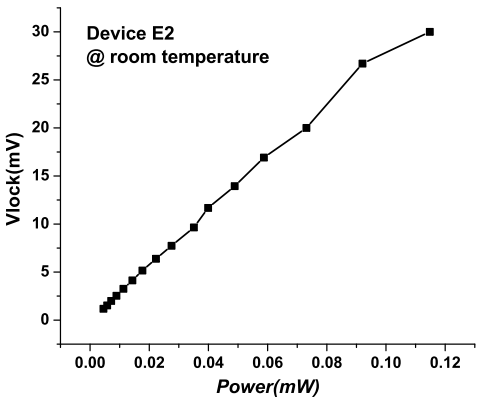

(e) Detection vs. microwave power level of device E2 at room temperature.

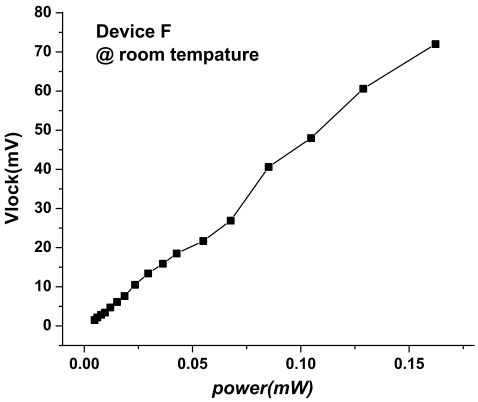

(f) Detection vs. microwave power level of device F at room temperature.

Figure 2.26. Microwave detection as a function of microwave power level of different devices.

with and without CNTs across the gap. So we can do a de-embedding process to get rid of the effects of the CPW. (More details about de-embedding will be presented in Chapter 3). Figure 2.27 shows the $|S11|$ of the CPWs which have CNTs across the gap. Figure 2.28 shows the S11 on smith chart.

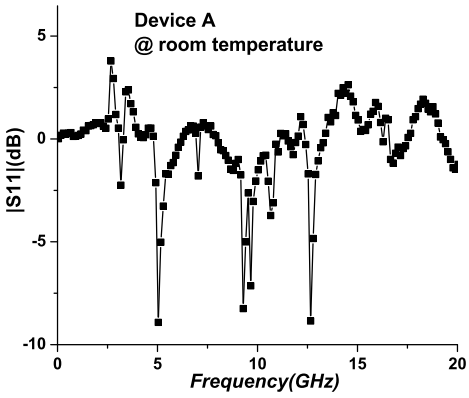

(a) Magnitude of S11 of device A at room temperature.

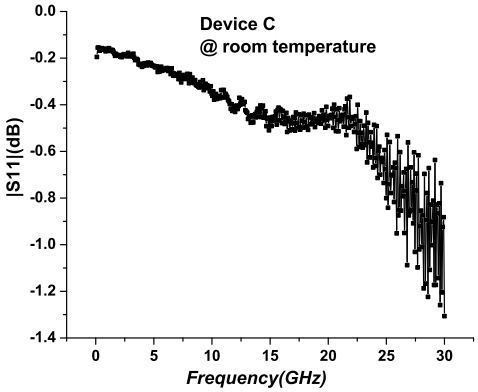

(b) Magnitude of S11 of device C at room temperature.

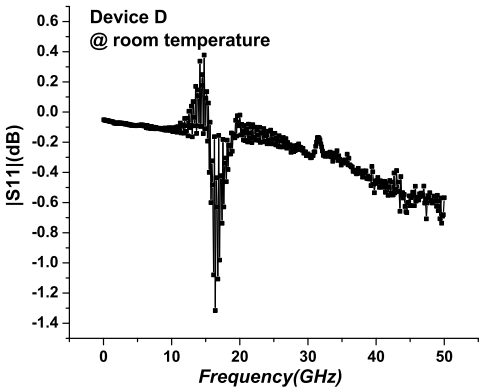

(c) Magnitude of S11 of device D at room temperature.

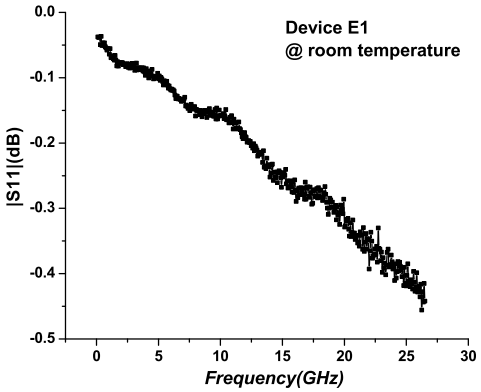

(d) Magnitude of S11 of device E1 at room temperature.

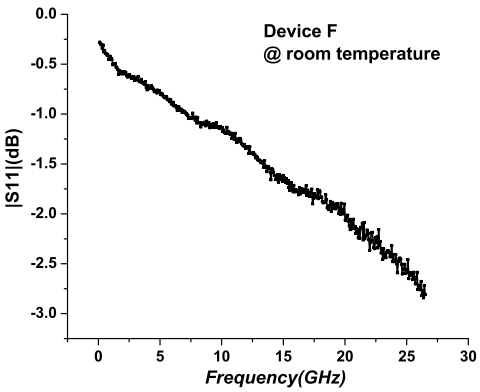

(e) Magnitude of S11 of device F at room temperature.

Figure 2.27. Magnitude of S11 of different devices.

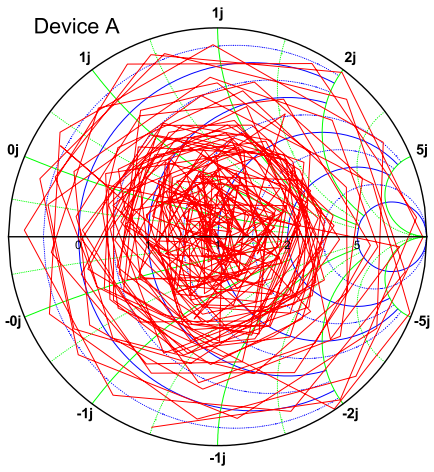

(a) Device A, calibrated at the SMA connector. Frequencies are from 45MHz to 20GHz.

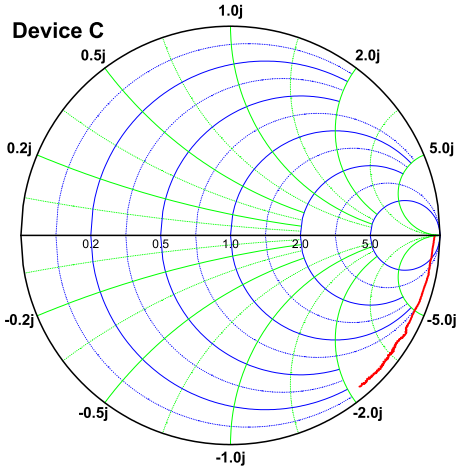

(b) Device C, calibrated at the end of the probe. Frequencies are from 45MHz to 30GHz.

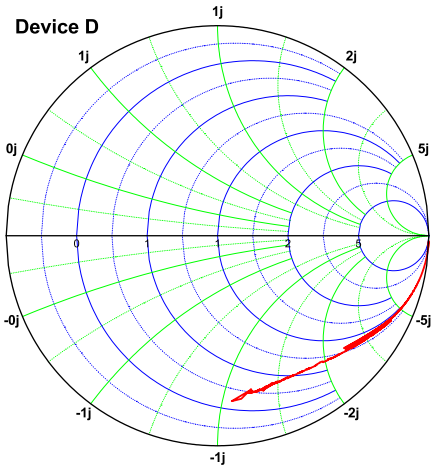

(c) Device D, calibrated at the end of the probe. Frequencies are from 45MHz to 50GHz.

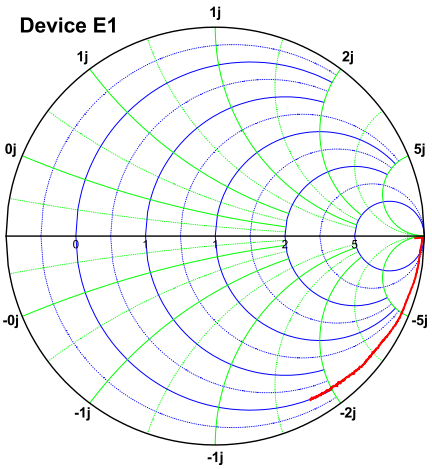

(d) Device E1, calibrated at the end of the probe. Frequencies are from 45MHz to 26.5GHz.

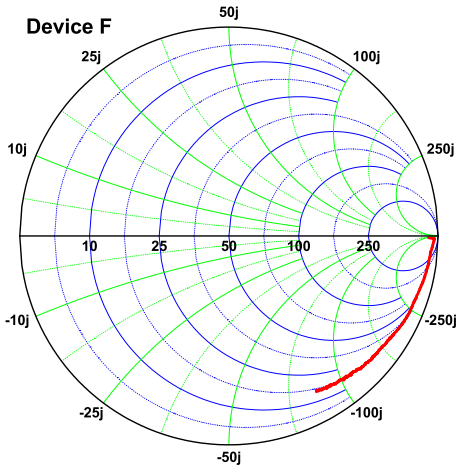

(e) Device F, calibrated at the end of the probe. Frequencies are from 45MHz to 26.5GHz.

Figure 2.28. The S11 parameter of different devices on smith chart.

CHAPTER 3

PHYSICAL PROCESS OF THE DETECTION

3.1 Terahertz detection process modeling

From the measurements data in Chapter 2, it is obvious that the terahertz detection of m-SWNTs is not following the second derivatives of the I-V curves of the CNTs. Therefore, a different detection process for the terahertz measurements needs to be proposed. First, it is useful to list the principal types of far infrared detectors, the categories in Table 3.1 are cited from ref. [52].

From Table 3.1, it can be seen that there is one group of detectors working at cryogenic temperature, it is the so-called bolometer detector. In this investigation, our hypothesis is that the detection process at terahertz frequencies is of the bolometric type, similar to that in ref. [60].

3.1.1 Bolometer Model

A bolometer, which was developed originally by Langley [89], is a device that has a temperature-dependent resistance R(T) and a heat capacity C_h. A bolometer consists of a radiation absorber and an electrical resistance thermometer coupled to a heat sink via a thermal conductance G_{th} [55], [90]. In some bolometers these two functions are combined in the same device.

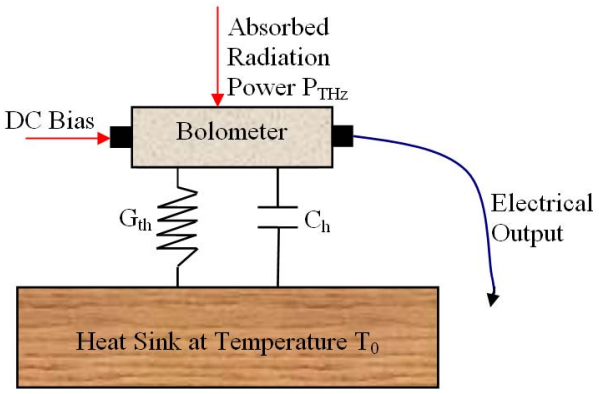

Figure 3.1. Diagram of the thermal bolometer detector.

Table 3.1. The principal types of far infrared detectors

Main	Sub-category	Instances	Refer to following reprints
Quantum Detectors	Photon Detectors	Diode Detectors	Saur;Putley; Moore and Shenker;Oka et al; Quist;Stillman;Arams et al
		Photovoltaic	
	Superconductucting Josephson effect		Grimes;Richards and Sterling;Grimes and Shapiro;McDonald et al
Thermal Detectors	Room Temperature	Pneumatic	Golay
		Thermistor bolometer	Wormser;Allen et al
		Thermocouple and thermopile	Stafsudd and Stevens
		Pyroelectric	Cooper; Hadni; Glass; Leiba
	Cryogenic	Carbon bolometer	Boyle and Rodgers
		Ge bolometer	Low; Blakemore; Oka et al; Zwerdling et al
		Si bolometer	Kinch
		InSb free-carrier-absorption bolometer	Putley; Kinch and Rollin; Kogan; Arams et al
		Superconducting bolometer	
Diode Detectors	Semiconductor		Young and Irvin; Stauch et al; Bechlake et al
	Metal		Daneu et al; Matarrese et al; Abrams and Gandrud

A generalized model of the thermal detector is shown in Figure 3.1. The heat equation for thermal detectors in its simplest form for a time-varying source of radiation is:

$$C_h \frac{d(\Delta T)}{dt} + G_{th}(\Delta T) = P_{THz} e^{\jmath\omega t} \tag{3.1}$$

Where

ΔT = temperature rise of detector element above the temperature T_0 of heat sink.

C_h = heat capacity of the thermal detector in joules/^oK.

G_{th} = thermal conductance between detector and heat sink.

P_{THz} = absorbed peak radiation power.

ω = angular modulation frequency of terahertz power.

The solution of the Equation 3.1 yields a steady-state amplitude:

$$\Delta T = \frac{P_{THz}}{G_{th}} \frac{1}{\sqrt{1+\omega^2\tau^2}} \tag{3.2}$$

Where

$$\tau = \text{time constant} = \frac{C_h}{G_{th}} \tag{3.3}$$

A key parameter in bolometers is the temperature coefficient of resistance b, defined by:

$$b \equiv \frac{1}{R}\frac{dR}{dT} \tag{3.4}$$

We will use the units '%/K' to quantify the factor b, so that the resistance change caused by the temperature change is:

$$\Delta R = R\ b\ \Delta T \tag{3.5}$$

Therefore, using Equation 3.2, the corresponding voltage change is:

$$\begin{aligned}\Delta V &= I_0\ \Delta R \\ &= I_0\ R\ b\ \Delta T \\ &= I_0\ R\ b\ \frac{P_{THz}}{G_{th}}\ \frac{1}{\sqrt{1+\omega^2\tau^2}}\end{aligned} \tag{3.6}$$

In this investigation, the dc bias is given by a programmable voltage source V_0 as described in Chapter 2, so ΔV can be rewitten as:

$$\Delta V = V_0\ b\ \frac{P_{THz}}{G_{th}}\ \frac{1}{\sqrt{1+\omega^2\tau^2}} \tag{3.7}$$

So the responsivity can be derived as:

$$S_V = \frac{\Delta V}{P_{THz}} = \frac{V_0\ b}{G_{th}}\ \frac{1}{\sqrt{1+\omega^2\tau^2}} \tag{3.8}$$

In the above derivation, we neglected the influence of thermal-electrical feedback, i.e. the temperature rise $\Delta T = P/G_{th}$ expected from an increase in radiant power P_{THz} is modified by the fact that R changes and, so the bias heating changes. We also assume that ω is low compared with $1/2\pi\tau_{th}$ for simplicity:

$$S_V = \frac{V_0\ b}{G_{th}} \tag{3.9}$$

Many materials do have an appreciable temperature dependence of their resistance, so the class of materials to consider is rather large. Clearly, we would like b to be large; an example of such materials is furnished by superconducting HEBs [63] for which b can easily be 100 $\%/K$ or greater, due to the sharpness of the superconducting

transition [30]. A different example is the 2DEG (Two Dimensional Electron Gas) medium in $AlGaAs/GaAs$ hetero-junctions. Here, b is of the order of 8 %/K at 77 K, and successful HEB direct and heterodyne detectors have been demonstrated with a thermal time constant of about 50 ps [91], later decreased by Lee et al., taking advantage of ballistic transport in short devices, to less than 5 ps [92]. It is also important to consider G_{th}, which can be large or small depending on the factors C_V, V and τ_{th}. For example, we can design a bolometer with a large S_V even if the volume is large and has a moderate b-value, provided that G_{th} is simultaneously low. However, that bolometer will react quite slowly (for example have a ms time-constant). Many sensitive bolometers are of this type. Clearly, there are many different ways of trading off the material properties of bolometers depending on what final performance we desire.

With the equations derived above, (3.9), we are able to justify the bolometer model using the temperature measurement data, shown in Figure 2.15. From the I-V curves, the resistance, R=V/I can be calculated at different temperatures. The results are shown in Figure 3.2.

In those curves, the temperature varies from 4.23 K (LHe), which is the uppermost curve, to 290 K (room temperature). Notice that all the curves show the zero-bias anomaly (ZBA), and for the ones at lower temperatures the ZBA is more observable. The resistance as a function of the temperature has already been shown in Figure 2.17, here, it is shown again for convenience in Figure 3.3.

Further, the differential change of the resistance with respect to temperature (dR/dT) can be derived as a function of the bias voltage, shown in Figure 3.4. Here, for clearness, only part of the temperatures are plotted in the figure.

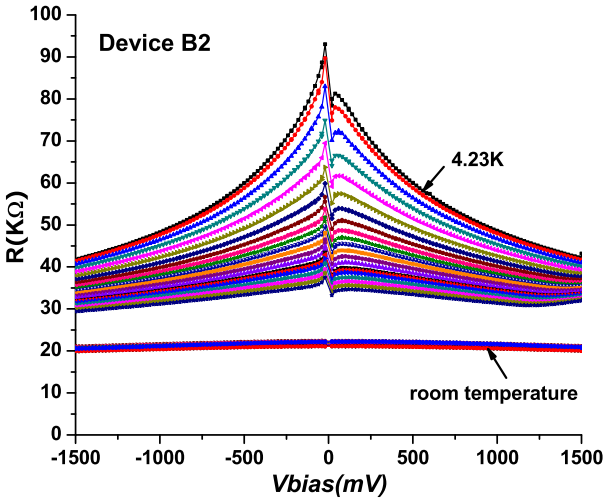

Figure 3.2. Resistances of device B2 as a function of bias voltage at different temperatures.

As defined ealier, the temperature coefficient b=$\frac{1}{R}\frac{dR}{dT}$, is shown in Figure 3.5.

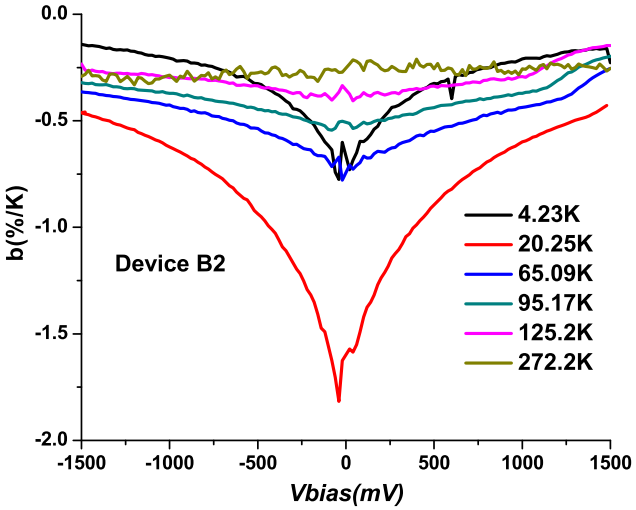

Figure 3.5. The temperature coefficient of device B2 as a function of bias voltage at different temperatures.

Now in the formula (3.9), we can insert measured values of V_0 and b, and only G_{th} is unknown. Here we assume that G_{th} remains constant at one temperature as V_{bias} varies. We will obtain an estimation value for G_{th} for different temperatures by fitting the expected responsivity (Sv) from the bolometer model (Eqn. 3.9) optimally

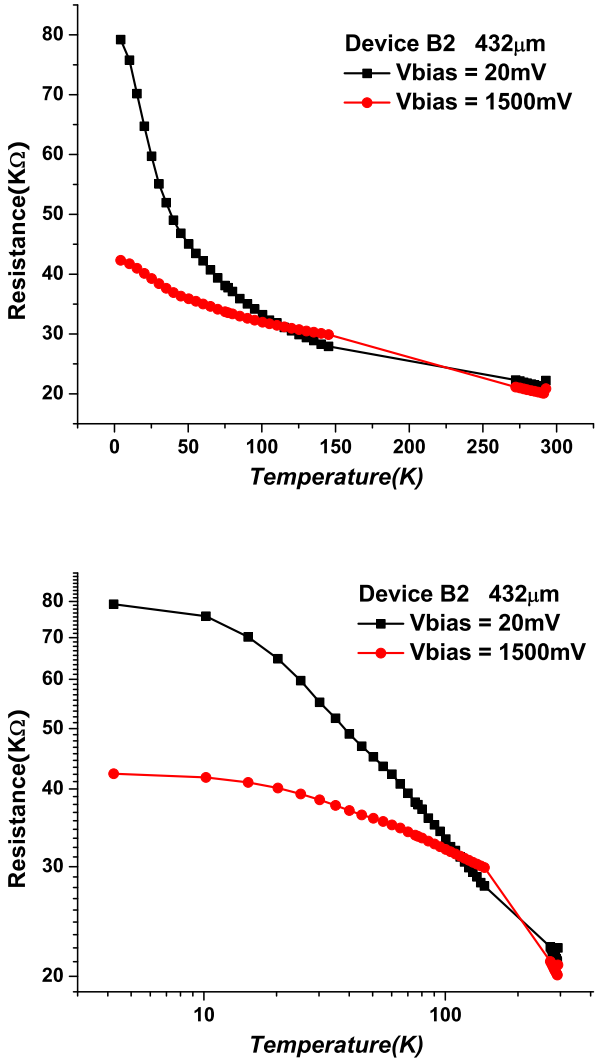

Figure 3.3. Resistances of device B2 as a function of the temperature both in linear scale (top) and log scale (bottom).

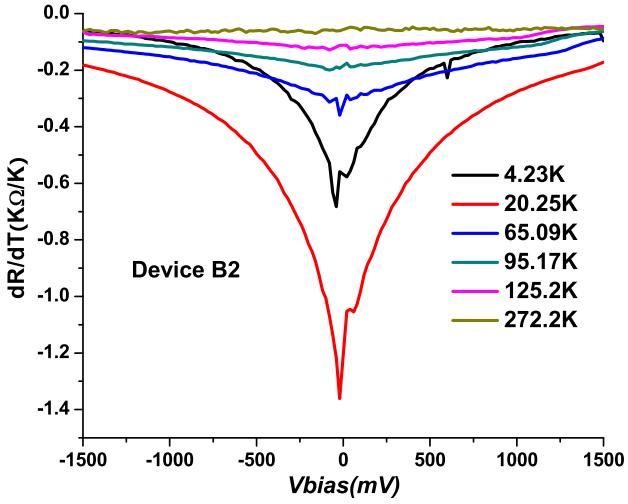

Figure 3.4. dR/dT of device B2 as a function of bias voltage at different temperatures.

to the experimental data, see Figure 3.6-3.11. All fits are very good except for Figure 3.11 (at 300K). The rationale for the estimated G_{th} will be discussed afterwards.

The values for G_{th} obtained from these fits are 2.13×10^{-3} W/K (77 K) and from 2.33×10^{-4} W/K to 6.75×10^{-4} W/K (4.2 K); If we compare the values of G_{th} obtained at different frequencies, see Table 3.2, these values are quite similar and consistent.

Table 3.2. Values of G_{th} obtained at different temperatures and frequencies

Temperature (K)	Frequency (THz)	$G_{th}\,(mW/K)$
4.23	0.694	0.233
4.23	1.05	0.31
4.23	1.63	0.675
4.23	1.63	0.276
77	1.40	2.13
300	1.40	70

The consistency depends on factors such as measurement of the THz power, optical coupling, etc. The plots of S_v in Figure 3.6 to Figure 3.11 refer again to the power outside the dewar, whereas equation (3.9) refers to the actual absorbed power. To correct for this we assume a total mismatch plus optical loss of about 16 dB. These

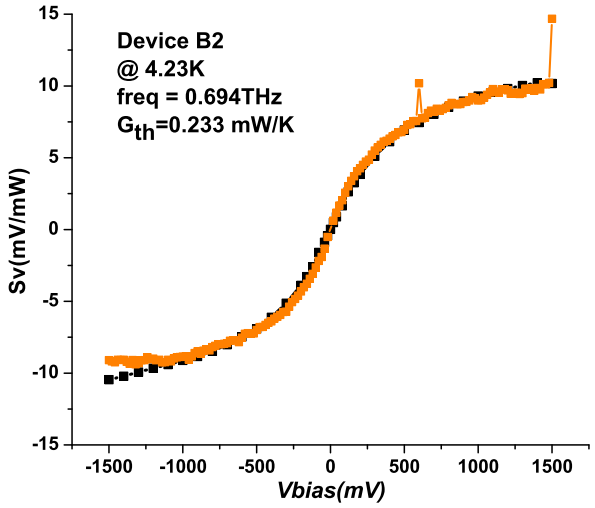

Figure 3.6. Comparison between the experimental data and the bolometer model data at 0.694THz, 4.23K.

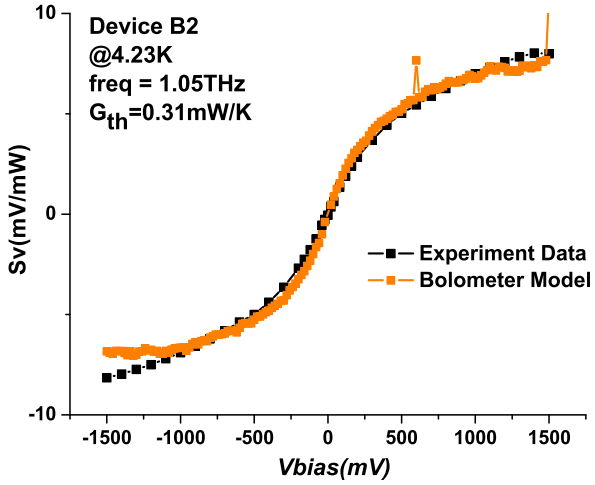

Figure 3.7. Comparison between the experimental data and the bolometer model data at 1.05THz, 4.23K.

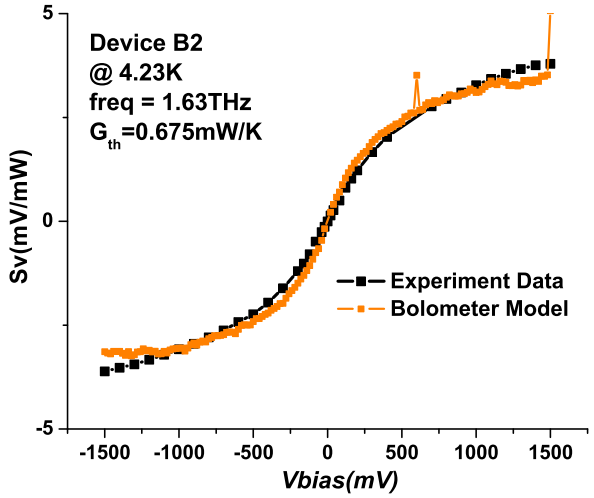

Figure 3.8. Comparison between the experimental data and the bolometer model data at 1.63THz, 4.23K.

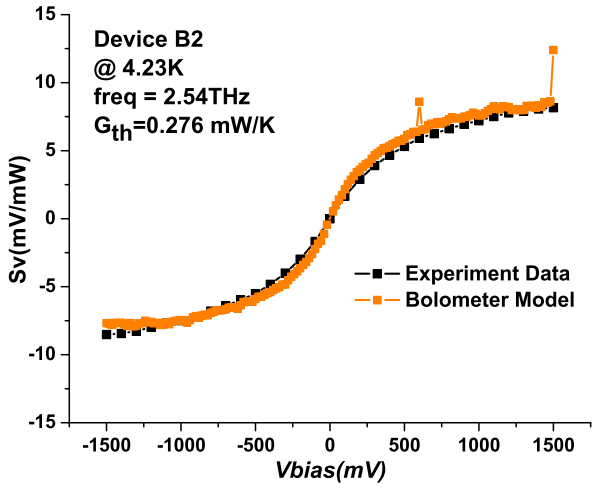

Figure 3.9. Comparison between the experimental data and the bolometer model data at 2.54THz, 4.23K.

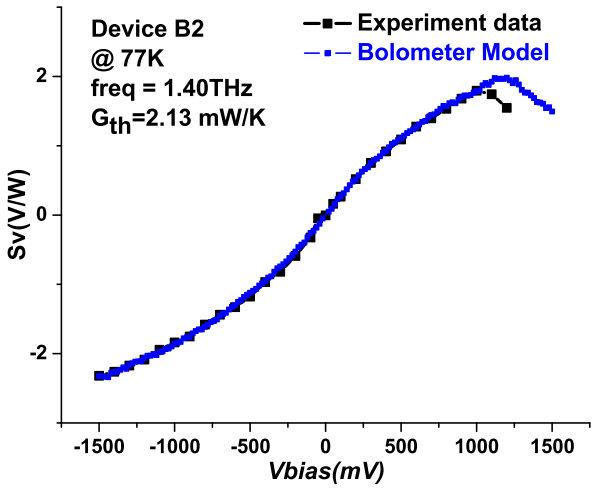

Figure 3.10. Comparison between the experimental data and the bolometer model data at 1.40THz, 4.23K.

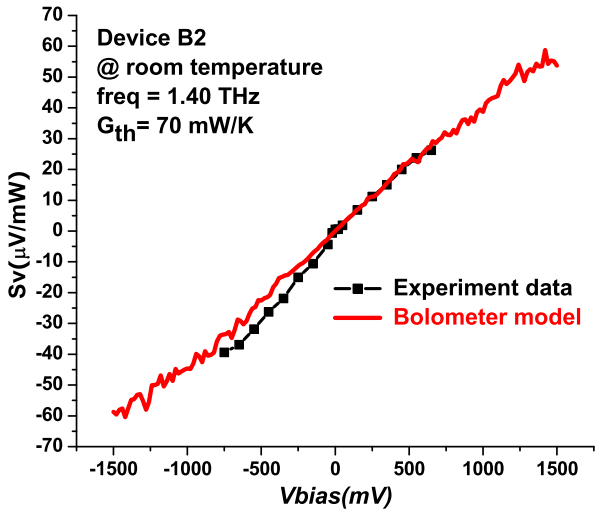

Figure 3.11. Comparison between the experimental data and the bolometer model data at 1.40THz, room temperature.

values will be justified later. The values for G_{th} then should be scaled down by a factor of 40 to 5×10^{-5} W/K (77K) and 6×10^{-6} W/K (4.2K). The 77 K value is within an order of magnitude of our theoretical estimates in Appendix A ($5.4 \times 10^{-6}\, W/K$), but larger. A larger G_{th} means a smaller ΔT, and a smaller S_V. The discrepancy in this direction may be ascribed to extra losses of terahertz power in the CNT bundles. The terahertz power may couple to other tubes contained in the bundles — s-SWCNTs, qm-SWCNTs and m-SWCNTs not well contacted at dc - neither of which contribute to S_V. Other possible coupling losses are discussed later. The effective coupling efficiency would then be lower, and G_{th} in better agreement. The estimate of the mismatch loss is of course also quite uncertain.

Based on our measured results, we can modify the general bolometer equation (3.9) as follows:

$$Sv = \frac{V_0\ b}{G_{th}}\left(\frac{\eta_{THz}}{L_{opt}\ L_{mism}}\right) \tag{3.10}$$

Here η_{THz} = efficiency of absorbed power for changing the bolometer resistance

L_{opt} = optical loss$\simeq$ 4 dB; this value is well known from earlier measurements on NbN HEBs

L_{mism} = mismatch loss between the antenna and the bolometer, to be discussed in Section 3.3.1

Equation (3.10) gives the responsivity of the SWNT bolometer with respect to power ourside the dewar. By performing fits such as above for a number of temperatures we can plot the T-dependence of G_{th}, see Figure 3.12. In plotting these curves we did not correct for η_{THz}, L_{opt} or L_{mism} which can be assumed to all be approximately independent of T. We can see that in log-log scale, G_{th} varies linearly with temperature up to about 35 K, and then varies more steeply. This is in agreement with expectations from theory, see [93]. The G_{th} fits worked well up to just over 100 K. At higher temperatures it is possible that other processes such as the diode process also contribute.

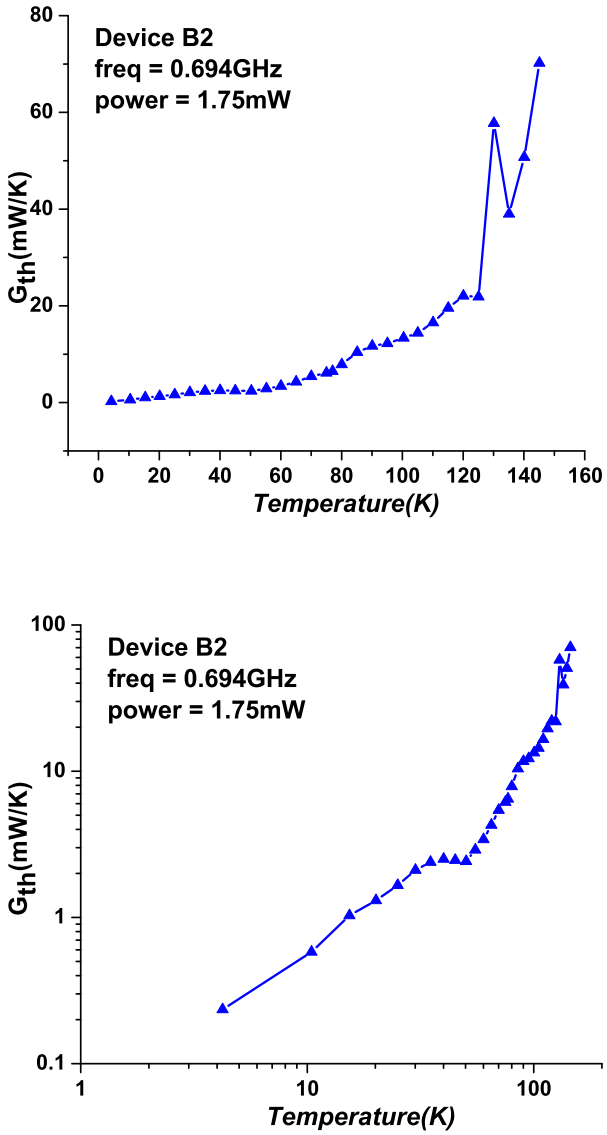

Figure 3.12. The T-dependence of the thermal conductance G_{th}.

We also measured the temperature dependence of the responsivity, see Figure 3.13. We should note that temperature dependence for devise A is much weaker (from 2 V/W at 77 K to 1.2 V/W at room temperature). Also device B1 showed some detection at 300 K, but it went from 5 V/W at 77 K to 0.2 V/W at 300 K.

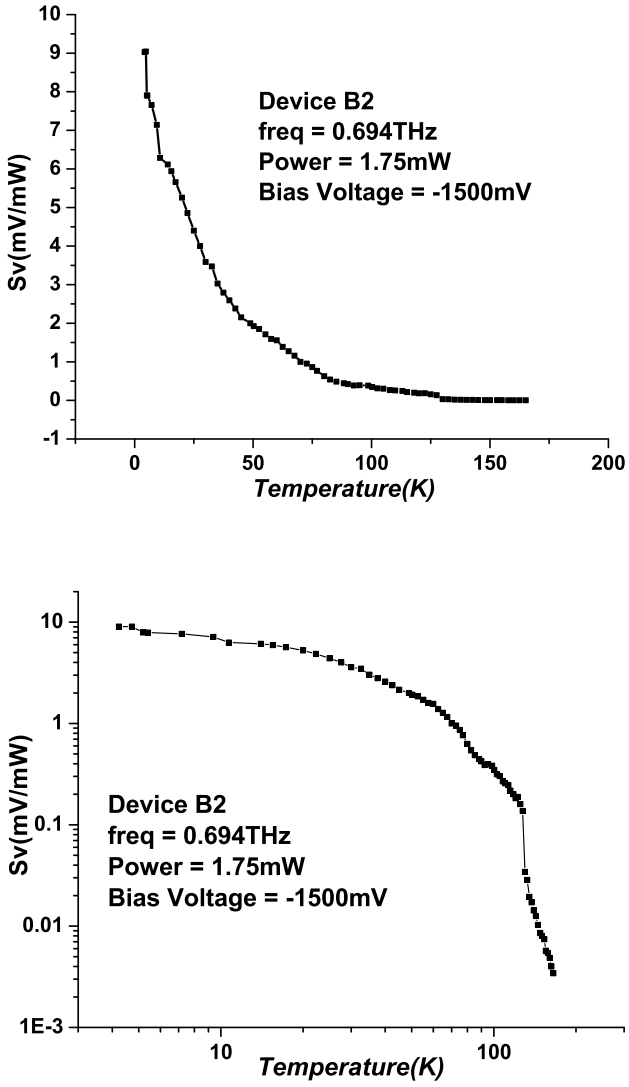

Figure 3.13. Responsivity with device B2 as a function of the temperature both in linear scale (up) and log scale (bottom).

The responsivity of device B2 drops quite slowly up to 60-70 K and then much more rapidly. Specifically, S_V has decreased by a factor of two at a temperature of

about 25 K which shows good potential for operation at higher temperatures than NbN HEBs, for example. The signal drops into the noise at about 160 K. We can understand the moderate temperature dependence of S_V if we refer to Figure 3.5 and 3.12. From Figure 3.12, G_{th} increases linearly with T (up to about 50 K), which would result in $S_V \propto \frac{1}{T}$. This is compensated partly by the fact that b also increases as is clear from Figure 3.5.

The thermal time-constant can be estimated from Eq. 3.3. We first must estimate the heat capacity C_h of the device (See Appendix A). We find the heat capacity to be 2.3×10^{-19} J/K for a $1\,\mu m$ long tube at 77 K [94], and 1.9×10^{-18} J/K for the $8\,\mu m$ long tubes in Device B. If we assume a total of ten tubes then $C_{tot} = 1.9 \times 10^{-17}$ J/K. With the value of $G_{th} = 5 \times 10^{-5}$ W/K from the above discussion we find that,

$$\tau_{th} = \frac{1.9 \times 10^{-17}}{5 \times 10^{-5}} = 0.38 \times 10^{-12}\, sec = 0.38\, ps \tag{3.11}$$

This is a very short time constant and corresponds to an IF bandwidth of 418.8 GHz for a heterodyne detector. We note that the value for G_{th} may be smaller by an order of magnitude, which would lengthen the thermal time-constant by an order-of-magnitude, though, as discussed on page 53. We can not yet perform direct measurements to estimate a value for τ_{th}. We modulate the laser at 1 kHz and find that the detected signal decreases when the modulation frequency is increased to the 5-15 KHz range, see Figure 3.14. This is consistent with the maximum rate at which our THz gas

laser can be modulated, as verified by using a Schottky diode detector, see Figure 3.15 [95].

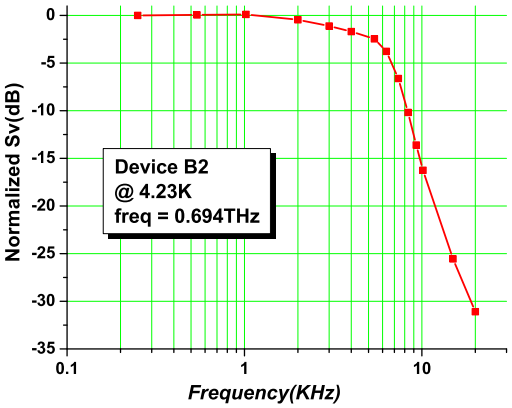

Figure 3.14. Measured responsivity of device B2 vs. the modulation frequency.

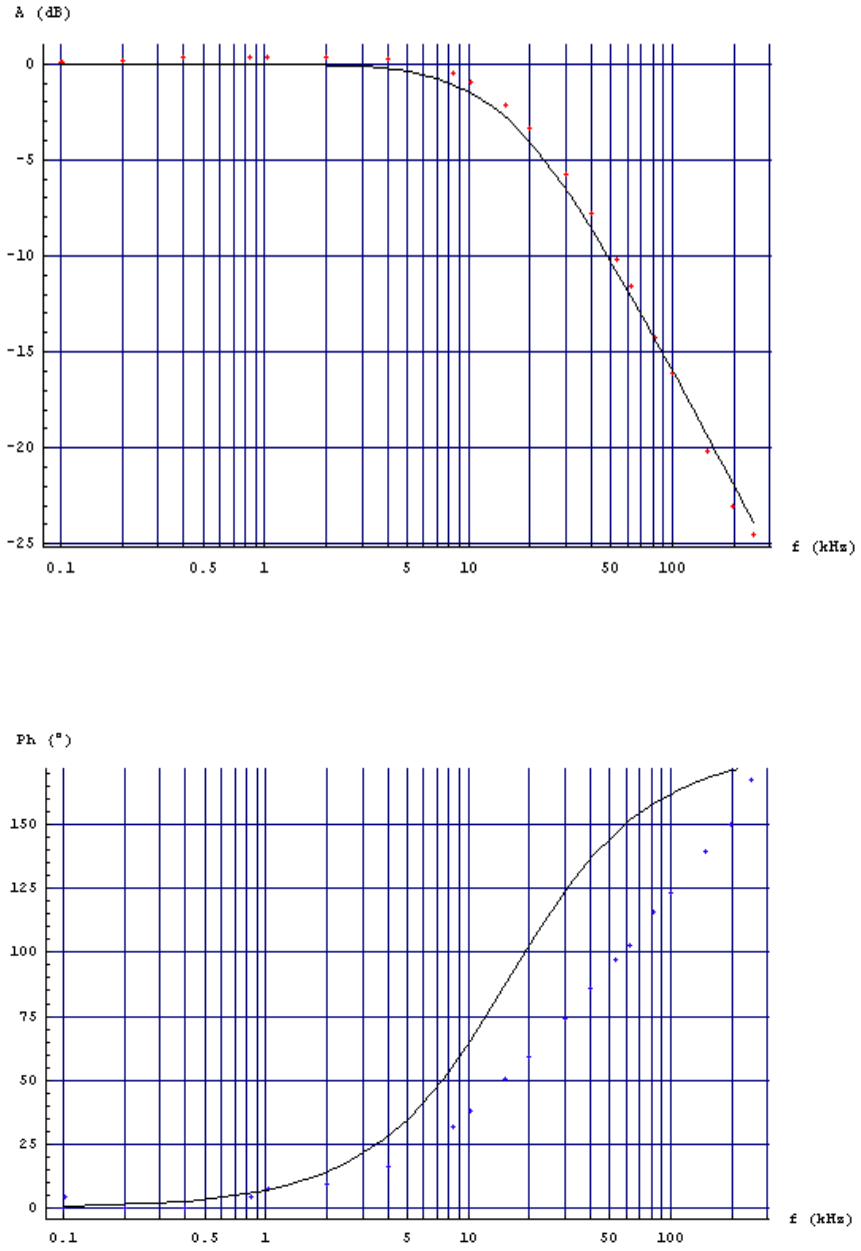

Figure 3.15. The FIR response versus modulation frequency of the THz laser in our lab[95].

3.2 Microwave data analysis

3.2.1 De-embedding process

To measure the microwave response (S11 parameter) of the carbon nanotubes, we need coaxial cables, probes and coplanar waveguide (CPW) structures. However, these additional elements also contribute to the measured S11 in a complicated frequency-dependent manner [96]. The removal of these undesirable parasitic signals is a very difficult task that has hindered many previous microwave characterizations of the CNTs. The parasitics introduced by the coaxial cables and the probes were removed using the well-known short-open-load (SOL) technique [97] using a standard calibration substrate. To remove the remaining parasitics generated by the CPW structure on which the CNTs get contacted, we employed a de-embedding technique that builds upon the Y matrix, and allows us to accurately remove the effects of the CPW structure.

The schematic of the probe and the CPW structure is shown in Figure 3.16, and the circuit model is shown in Figure 3.17. The CPW structure is basically a lumped element with mainly capacitive reactance and this element is in parallel with the carbon nanotubes, so it is reasonable and convenient to use the Y matrix representation of both of them.

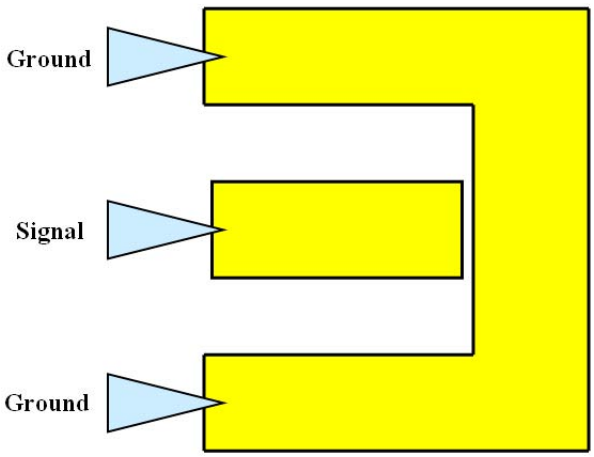

Figure 3.16. Schematic of the microwave probe with the CPW structure.

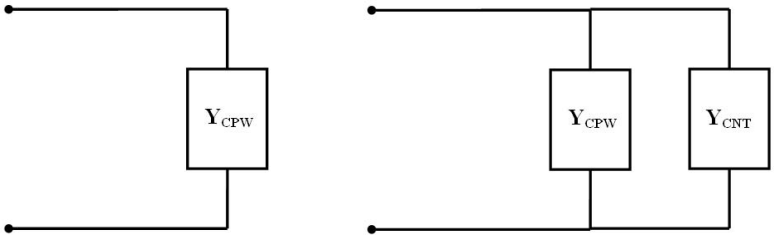

Figure 3.17. Circuit model of the CPW structure with(left) and without DUT(right).

The Y parameter matrix of the DUT can be easily obtained using

$$[Y]_{DUT} = [Y]_{meas} - [Y]_{CPW} \tag{3.11}$$

where $[Y]_{meas}$ is the (known) [Y] matrix obtained from the measured [S] parameter with carbon nanotubes connected across the gap of the CPW, and $[Y]_{CPW}$ comes from the measured [S] parameter without carbon nanotubes crossing the CPW gap. Then the Z parameter matrix of the DUT can be derived from

$$[Z] = [Y]^{-1}$$

3.2.2 De-embedding results

In this work, the de-embedding method has been applied to devices C, D, E1 and F. Among these devices, only device F is a planar log-periodic antenna (LPA), the others are coplanar waveguide (CPW).

The de-embedded [Z] parameters for different devices of the CNTs are shown in Figure 3.18-3.21.

3.2.3 Circuit model

With the de-embedded S or Z parameters, we can try to fit it into a circuit model which is shown if Figure 3.22. In the above model, the contacts are represented by parallel RC pairs, and an inductor with a resistor in series represents the bulk of the

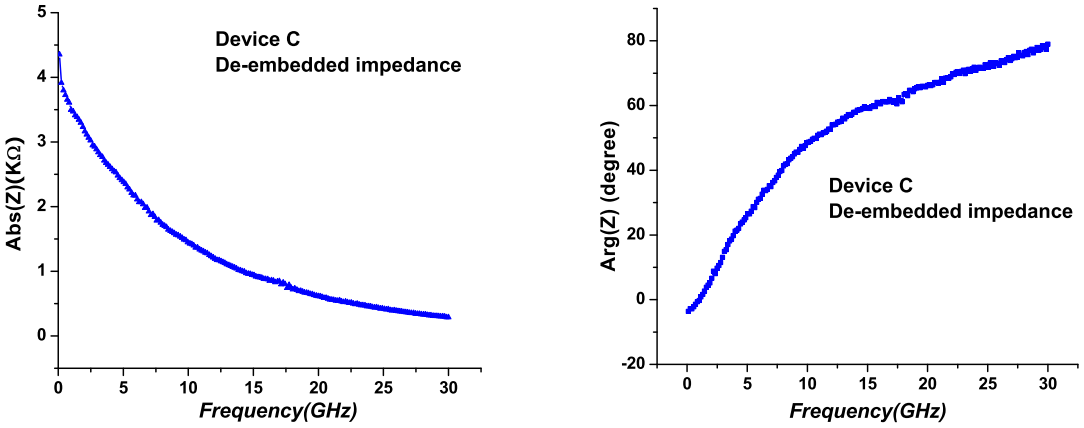

Figure 3.18. De-embedded impedance of CNTs in device C.

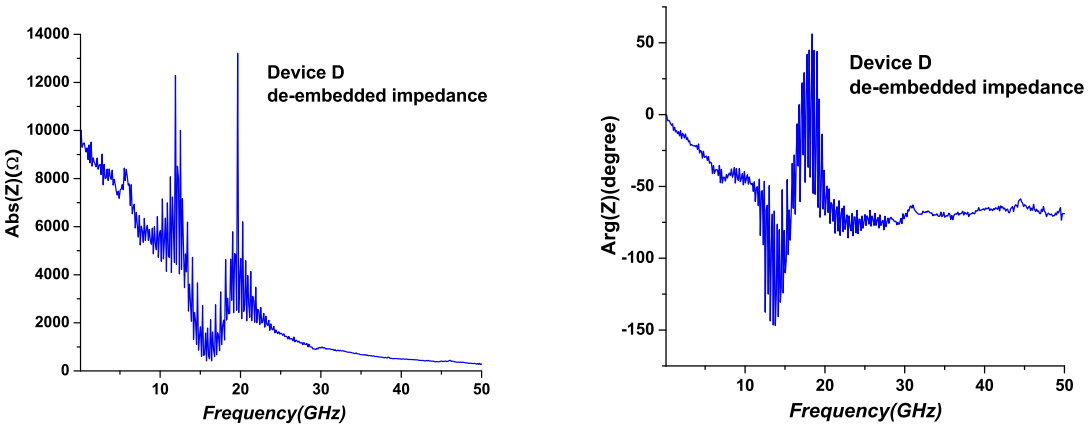

Figure 3.19. De-embedded impedance of CNTs in device D.

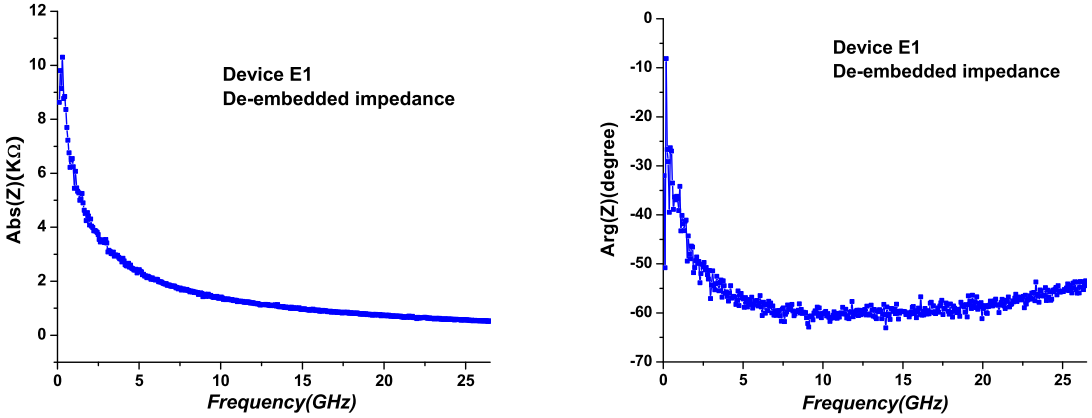

Figure 3.20. De-embedded impedance of CNTs in device E1.

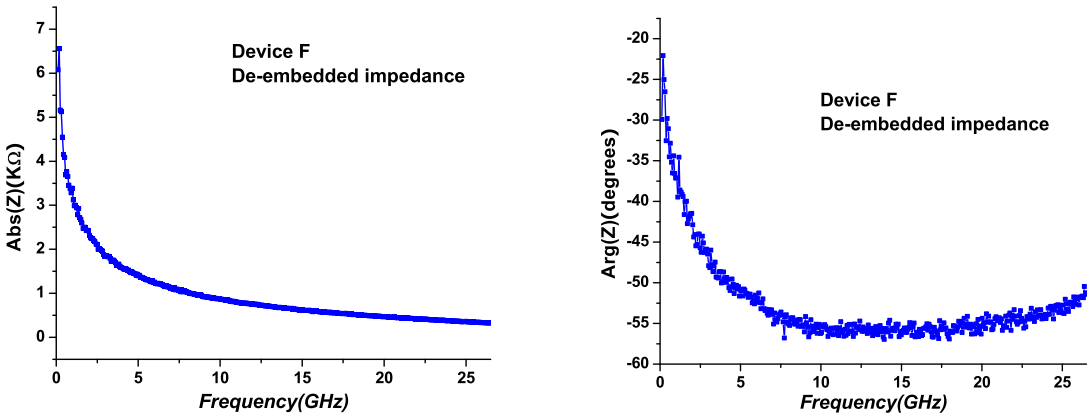

Figure 3.21. De-embedded impedance of CNTs in device F.

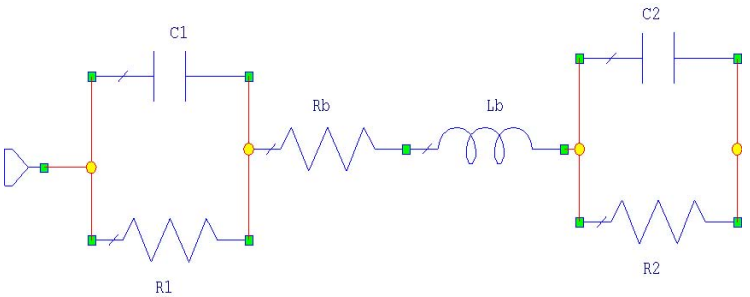

Figure 3.22. The circuit model used in this work to fit the de-embedded data.

bundle; the model used here is also used by other groups [46], [98]. In this work, we assume that the properties of the two electrode-bundle contacts are different, which is supported by the results of Ref. [99].

The de-embedded impedance versus frequency curves with their circuit fits are shown in Figure 3.23-3.26.

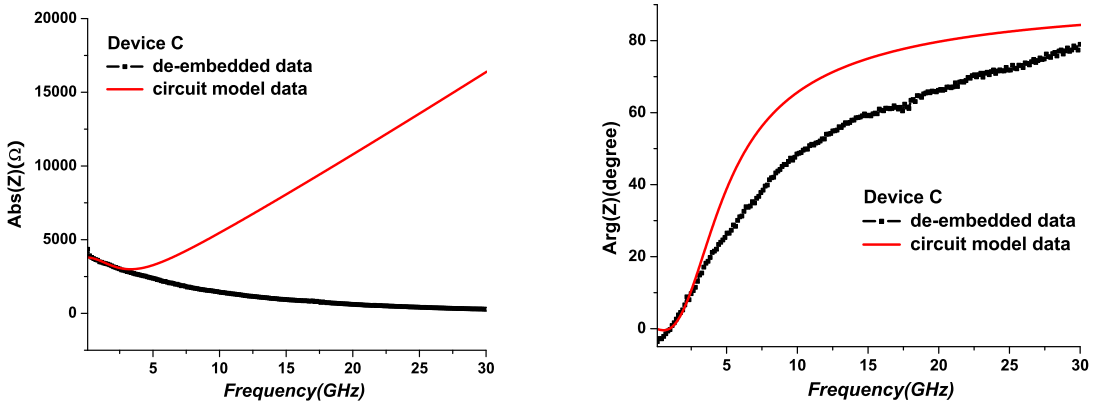

Figure 3.23. De-embedded impedance versus frequency with the circuit fits of CNTs in device C.

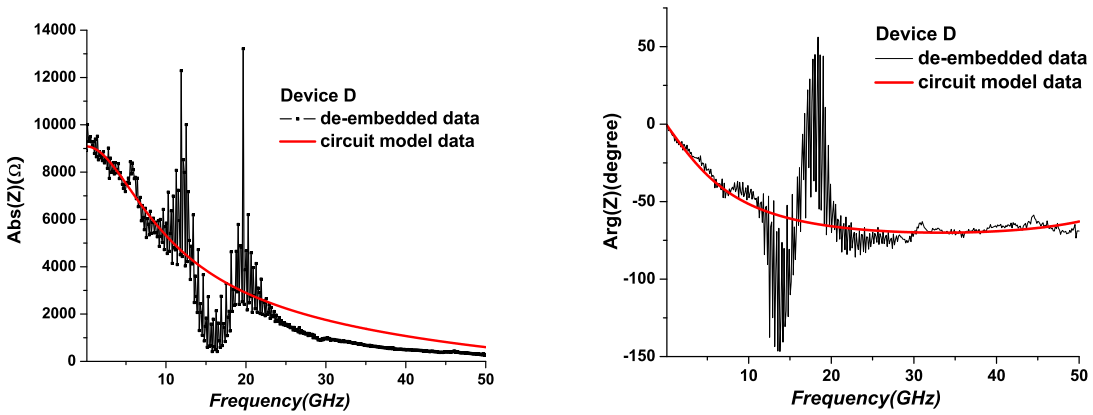

Figure 3.24. De-embedded impedance versus frequency with the circuit fits of CNTs in device D.

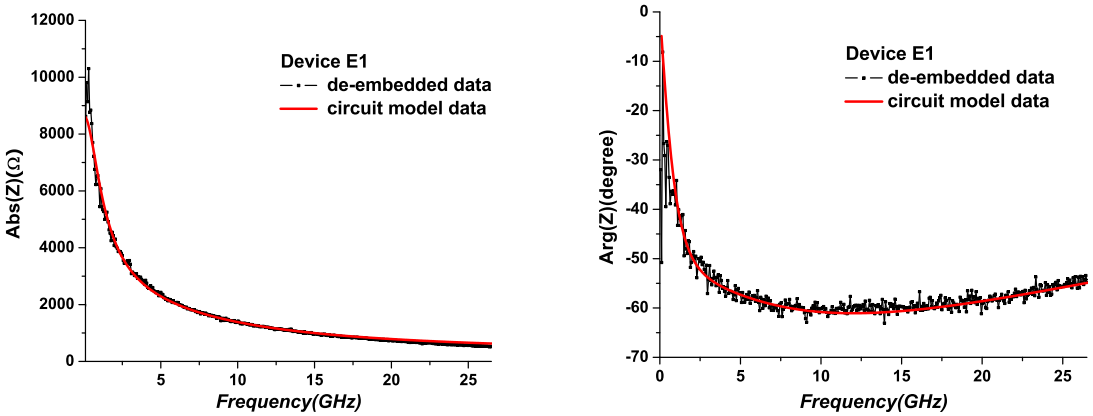

Figure 3.25. De-embedded impedance versus frequency with the circuit fits of CNTs in device E1.

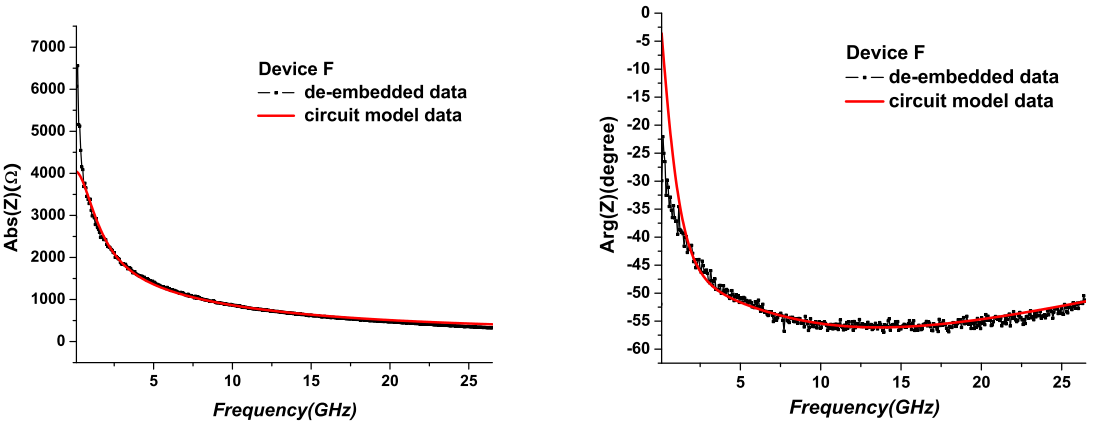

Figure 3.26. De-embedded impedance versus frequency with the circuit fits of CNTs in device F.

For device C (Figure 3.23), we only get reasonable fits up to 3 GHz, and beyond that, it is impossible to fit it using our circuit model. It is due to the complex coupling effects between different carbon nanotubes and between different bundles. For device D, there is a resonant-like behavior between 10 GHz and 20 GHz range. However, this is not the real characteristics of the CNT since it is also seen in the data of measured empty CPW structures. So it is most likely due to the calibration error at these frequencies. When we do the circuit model fit, we just ignore the resonance in that frequency range. For device E1 and F, however, we get reasonably good fits up to 26.5 GHz. The extracted values of the lumped elements are summarized in Table 3.3. From the table, it can be seen that most of the dc resistance distributes in the

Table 3.3. Extracted values of the lumped elements in the circuit model.

Device	Rb (kΩ)	Lb (nH)	R1 ($k\Omega$)	R2 ($k\Omega$)	C1 (fF)	C2 (fF)
C	0.34	92	1.94	1.52	2	42
D	0.08	2.50	4.28	4.73	4.96	4.50
E1	0.29	0.03	1.06	7.29	23.4	21.6
F	0.20	0.05	0.61	3.25	32.4	37.5

contacts. For device E1 and F, the kinetic inductance (Lb) is very small compared to the theoretical value, 4nH/μm (the gap of the CPW is around 4μm). This implies that there is a large amount of tubes in parallel.

With the fitted circuit model, the trend of the detection of the CNTs versus frequency can be estimated by calculating the voltage drop across the contact resistances as a function of frequency, see Figure 3.27-3.30. Here, we assume the detection at microwave frequencies is due to the diode process. Thus, it is the nonlinearity of the contact resistances which contribute to the detections. In discussing the model fits in Figure 3.27 to 3.30, we first note that the model does not provide a good fit to the measured S11 data for Device C. The model predicts that the responsivity should fall rapidly above about 8 GHz, where as the measured data in Figure 2.24(b) are essentially independent of frequency. This device is likely to have a more complex

structure that can not be fitted to the model. It is interesting that nevertheless the measured responsivity is independent of frequency up to 20 GHz, a general feature for all devices. In the case of Devices D, E1 and F this is also the behavior predicted by the model (with at most a 1-2 dB discrepancy).

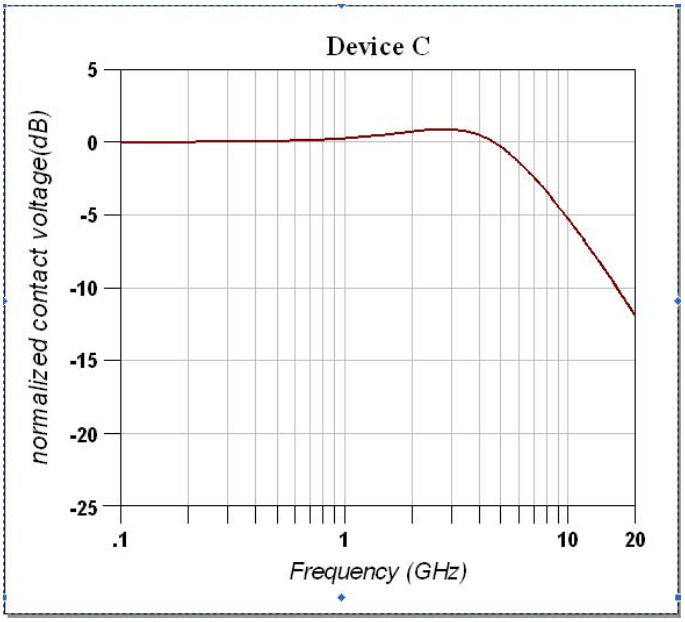

Figure 3.27. The normalized contacts voltage versus frequency of device C predicted by the circuit model.

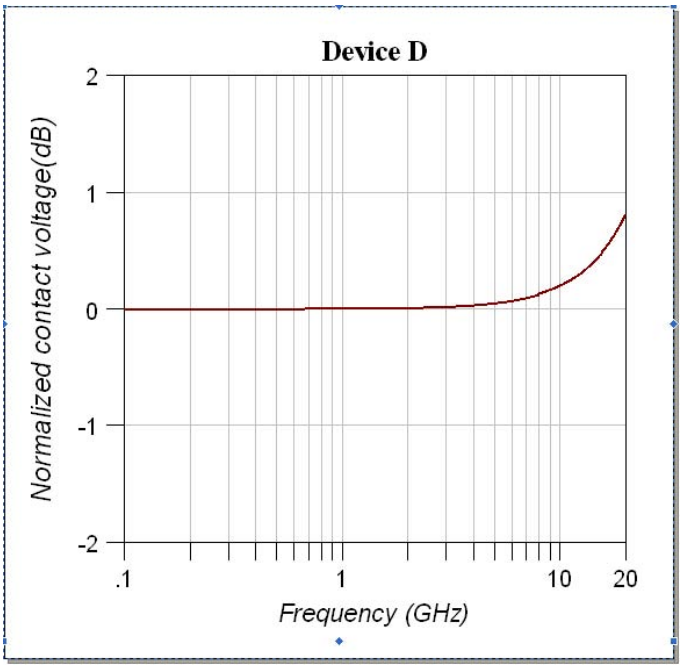

Figure 3.28. The normalized contacts voltage versus frequency of device D predicted by the circuit model.

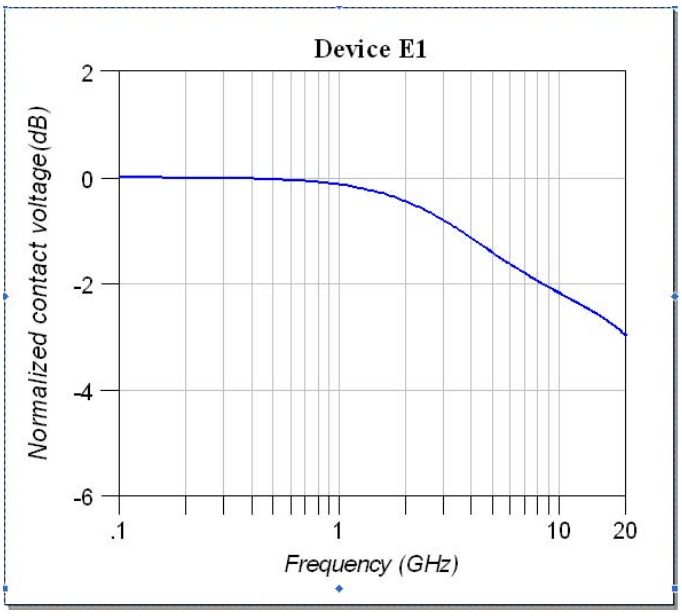

Figure 3.29. The normalized contacts voltage versus frequency of device E1 predicted by the circuit model.

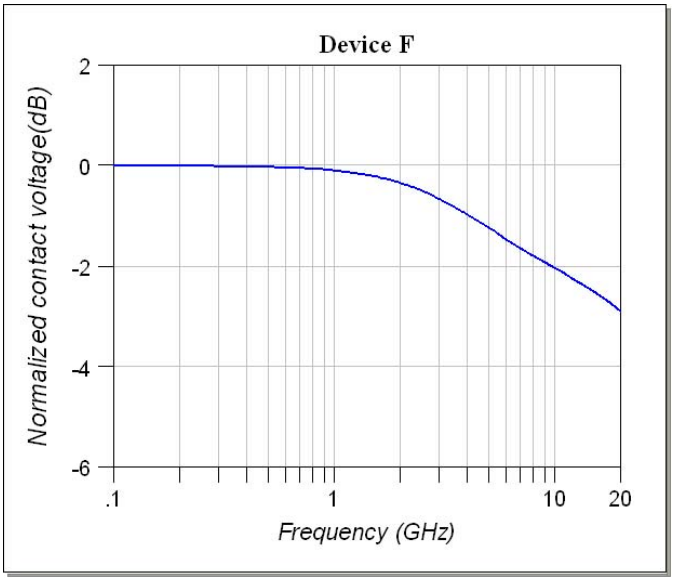

Figure 3.30. The normalized contacts voltage versus frequency of device F predicted by the circuit model.

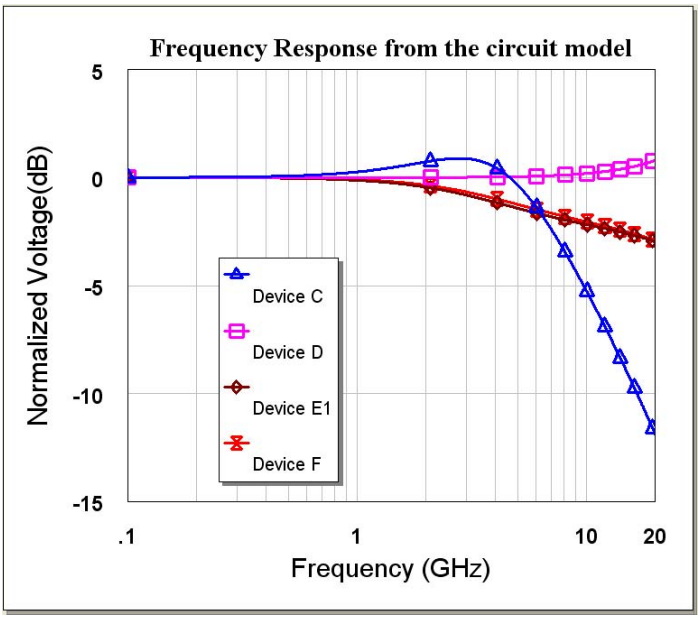

Figure 3.31. The normalized contacts voltage of different devices.

3.3 Consequences of the circuit model for the terahertz detection process

3.3.1 Terahertz absorption in the CNTs

The work by Itkis et al. [60] (as well as others) has shown that the CNT films have a broad absorption peak at close to 3 THz, due to quasi-metallic (QM) CNTs (qm-SWNTs) that have very small bandgaps (a few meV). The absorption coefficient is about the same as in the Near IR range. It is thus clear that at least these qm-SWNTs can absorb the terahertz radiation efficiently.

Single m-SWNTs (strictly metallic, not QM) are assumed to have an equivalent circuit as shown in Figure 1.5. To predict the terahertz properties of this circuit we will model the m-SWNT as a transmission line, rather than the lumped circuit of Figure 3.22. Our microwave measurements find values of the contact capacitance 2-40 fF. The capacitance is so large that it effectively shunts the contact resistance at THz frequencies. The equivalent circuit at THz then consists of the transmission line (TL) in Figure 1.5 only, and this TL has a characteristic impedance of about 10 KΩ. There is a mismatch loss between the TL and the antenna impedance (about 100Ω) of about 14 dB. If the Tomonaga-Lüttinger liquid plasmon resonances are not very strongly damped, the real part of the CNT impedance may be higher at these frequencies, resulting in the coupling becoming periodically lower [41]. However, at frequencies between these resonances the CNT impedance is still about 10 KΩ [41]. We have chosen the option of decreasing the mismatch loss by employing (many) bundles of parallel SWNTs. We employ an approximate model of Device B2 in which we assume that we have effectively ten tubes in parallel, each described by the TL circuit. We also assume a random variation of the length of the tubes. A simulation with this model then gives the result shown in Figure 3.31. We have assumed two different values for the intrinsic resistance of each CNT, 40 KΩ and 100 KΩ. For the latter value, the resonances are well damped, and the average mismatch loss (1 -

$|S11|^2$) is about 12 dB. This value was used in Equation (3.10) in our discussion in Section 3.1.1.

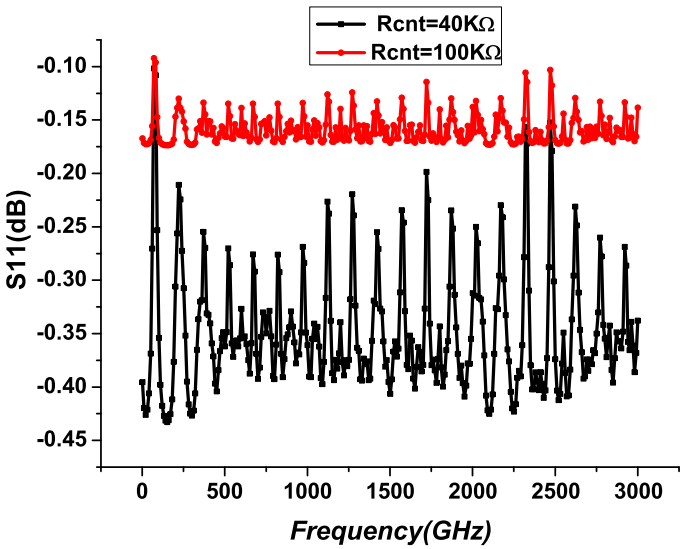

Figure 3.32. Simulation of S11 for a TL model of a ten tube m-SWNT bundle. The contact resistances are assumed to be shorted by the contact capacitances

Adding the optical loss of about 4 dB discussed earlier we find a total optical plus mismatch loss of 16 dB.

3.3.2 Mechanism of the change of the resistance

As the temperature increases due to terahertz heating of the CNTs, heated electrons diffuse or travel ballistically to the positive terminal contact and tunnel to its metallic contact pads. This decreases the resistance R just as happens when the entire device is heated thermally, and justifies our use of the dR/dT that was measured at DC. Note that R(T) is also due to tunneling of electrons to the contact pads. It is possible that the terahertz heating is less efficient than thermal heating of the entire device, and if that is the case then this effect can be included in η_{THz}, in Equation (3.10).

The discussion in Section 3.3 then completes a tentative physical model for the terahertz process in our CNT devices that is consistent with all experimental data. Future research is needed to confirm (or possibly refute) this model.

CHAPTER 4

FUTURE WORK

4.1 Terahertz detection

In this work, the performances of the SWNTs as a detector at terahertz and microwave frequencies are investigated. At terahertz frequencies, the common quasi-optical method is employed and detections on SWNTs were demonstrated for the first time. A bolometer model of the detection process was proposed based on the experimental data. The bolometer model fits the experimental data quite well at least at cryogenic temperatures. Beyond the scope of this investigation, there are more interesting aspects of the SWNTs at terahertz region that need to be explored and verified.

4.1.1 Detections on the short-gap antenna

The log-periodic antenna (LPA) used in this work has reasonably good performance up to 2.54 THz with a gap width of $8\,\mu m$. In the next step, a better antenna mask, that performed well in the NbN experiments of our group, could be employed, see Figure 4.1. The gap of this mask is $1\,\mu m$, and the antenna has well defined small tooth branches, which dominate the high frequency behavior of the antenna. With this antenna, higher THz frequency data could be collected and make the detection of the resonance of the 'Lüttinger Liquid' possible [41].

However, with such a small gap, a considerably diluted solution of the nanotubes needs to be used to prevent putting the CNTs over the entire center region of the antenna.

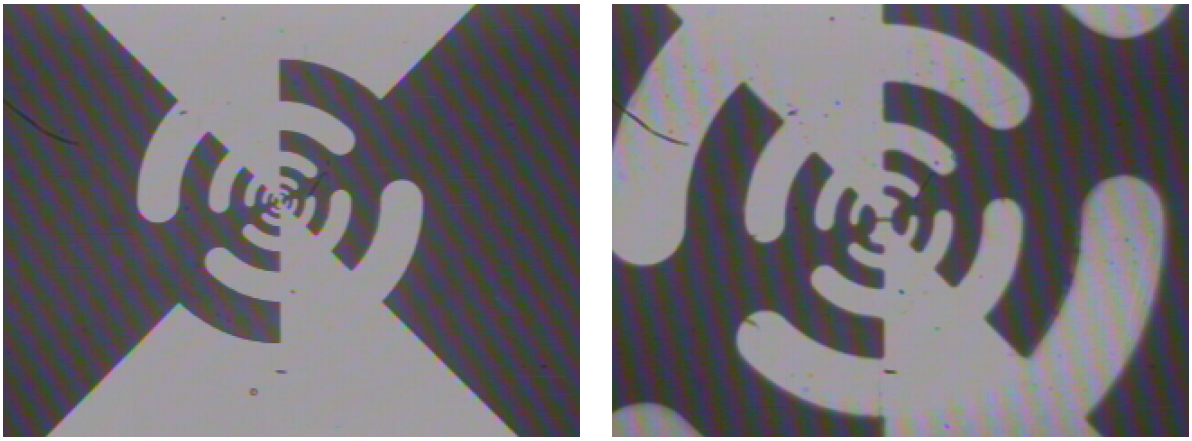

Figure 4.1. The photograph of the 1-μm gap mask.

4.1.2 Detection on Suspended SWNTs

In this work, a bolometer model was proposed to explain the experimental data of the terahertz detection. In this model, an important factor is the thermal conductance between the CNTs and the substrate (sapphire or silicon on sapphire in this work). It is highly desired to minimize this thermal conductance. It is natural and essential to design experiments to verify the terahertz detection when the CNTs are suspended. From another group's data [60] in the near infrared region, the responsivity will increase a lot with a similar temperature coefficient, b. In that case, the lateral thermal conduction was decreased by an especially large factor since heat had to be transported through many CNT junctions in a network. In our case the expected factor by which the responsivity will increase is much less, but still a factor of two or three orders of magnitude may be possible. The suspended CNTs can be made by etching the substrate between the gap [100], see Figure 4.2.

4.1.3 Heterodyne detection on SWNTs

It is predicted in theory that the IF bandwidth of heterodyne terahertz detection on m-SWNTs can be as wide as several hundred gigahertz [49]. It is extremely interesting to verify the theory by doing a heterodyne terahertz detecion. This experiment

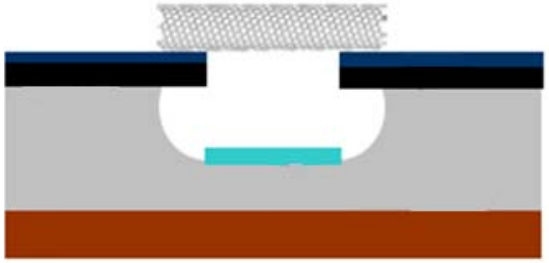

Figure 4.2. Diagram of the suspended tubes, Ref[100].

will require two terahertz sources tuned to frequencies separated by about 10 GHz. Since in the gigahertz range, the lock-in amplifier stops working, the detected signal needs to be amplified by a low-noise amplifier (LNA) as used in the NbN HEB hyterodyne detection in our group. The LNA we used has a bandwidth of 11 GHz, 20-30dB gain and extremely low noise temperature, about 3K. To really measure the IF signal up to 100 GHz, a second or even a third on-chip tunable integrated down converters is needed to translate the IF frequencies to the LNA band (0.5–11GHz) and the antenna mask needs to be re-designed to guide the millimeter wave IF signal properly to the input of the on-chip down-converter. In the future, it is anticipated that even wider versions of our MMIC cryogenic amplifier will be available.

4.2 Microwave measurements

Direct and heterodyne detections on SWNTs at microwave frequencies was demonstrated in our group [47] and also other groups before this thesis work. In the current investigation, direct microwave detections were performed up to much higher frequencies and the more accurate probe measurement was employed. Further, in this work, the microwave data were used for fitting the circuit model of the SWNTs. Rough estimations of the values of the circuit elements have been derived from the experimental data. The microwave investigation of SWNTs, like the terahertz detection, just started. Many more applications and research need to be done in the future.

4.2.1 More accurate on-wafer microwave measurements and de-embedding method

Microwave S parameter measurements of very high resistance devices as CNTs are difficult due to the large mismatch between source and device. The large uncertainties lies in the measurement itself and the de-embedding procedure always discredit the results [66]. Thus an accurate microwave measurement and de-embedding method is highly desired. To make better microwave measurements, with less calibration error, it is best to have custom designed calibration standards with the same substrates as the devices under test. To minimize the interferences from AM, FM radios, the cellular phones and the wireless networks, proper shielding is preferred for the calibration and measurement.

To make a more accurate de-embedding procedure to get the real response of the CNTs, a full set of two-port S parameter measurements, including reflection and transmission, is needed. The detailed procedure is in Ref [96].

4.2.2 Microwave probe measurements at cryogenic temperatures

It is also interesting to make S parameter probe measurements at cryogenic temperatures. It is useful to examine whether the resistance changes of the CNTs are caused by the resistance change of the contact or not. To do this cryogenic measurement, a well designed holder is needed to contain the liquid nitrogen or liquid helium, and to hold the chip under test [101].

APPENDIX

CALCULATIONS OF THERMAL CONDUCTANCE AND HEAT CAPACITY

(1) Estimation of G_{th}

Pop et al. [102] estimate a quite large thermal conductance per unit length of 0.17 $WK^{-1}m^{-1}$ from m-SWNTs to silicon substrates with an oxide layer, when the SWNTs are resting on the substrate. Maune et al. [103] found $G_{th} = 0.26\,WK^{-1}m^{-1}$ for sapphire substrates. Both papers used a thermal model that was fit to measured data of IV-curves. We assume that the thermal conductance for m-SWNTs on other similar substrates is close to this value. It is interesting to note from ref. [102] that G_{th} can be varied from its low value for suspended tubes by allowing gases to contact the CNT, or by allowing CO_2 gas to condense between the CNT and the substrate at low temperatures. Since our tubes can be assumed to touch the sapphire (or SOS) substrate, we assume that G_{th} (per unit length) $= 0.26\,WK^{-1}m^{-1}$. The length of the tubes is about 8 μm, so $G_{th} = 2.1 \times 10^{-6}\,W/K$ for a single tube. If we estimate that we have the equivalent of ten tubes in parallel, $G_{th} = 2.1 \times 10^{-5}\,W/K$ at 300 K. We can assume that G_{th} varies linearly with temperature when the temperature is not too low, and thus $G_{th} = 5.4 \times 10^{-6}\,W/K$ at 77 K. This value was quoted on page 57 and compared there with the values derived from fits to the measured data.

(2) Estimation of the heat capacity of an m-SWNT

From Ref. [94], the heat capacity for 1-D structure can be expressed as:

$$C_V^{1D} = 2\pi^2 L k_B^2 T/3h\nu$$

Here, L is the length of the tube, k_B is the Boltzmann constant $= 1.38 \times 10^{-23} J/K$, T is the temperature in Kelvin, h is the Plank constant $= 6.63 \times 10^{-34} J \cdot s$ and ν is the acoustic phonon velocity, here we use $1.5 \times 10^4 m/s$.

So the heat capacity of one carbon nanotube per unit length is:

$$C_V = 5.82 \times 10^{-14} JK^{-1} m^{-1}$$

In our case, the length of the carbon nanotube is $8\mu m$, and we consider four propagation modes. The heat capacity of an individual carbon nanotube becomes:

$$C_h = 1.86 \times 10^{-18} JK^{-1}$$

This value was used in our estimation of the thermal time constant of the devices on page 60.

BIBLIOGRAPHY

[1] A. M. Ionescu and K. Banerjee, *Emerging Nanoelectronics–Life with and after CMOS*. Norwell, MA: Kluwer Academic Publishers, 2005.

[2] "National nanotechnology initiative," http://www.nano.gov.

[3] G. D. Wilk, R. M. Wallace, and J. M. Anthony, "High-$\mathcal{K}$ gate dielectrics: Current status and materials properties considerations," *Journal of Applied Physics*, vol. 89, no. 10, pp. 5243–5275, May 2001.

[4] M. L. Green, E. P. Gusev, R. Degraeve, and E. L. Garfunkel, "Ultrathin (<4 nm) SiO_2 and Si-O-N gate dielectric layers for silicon microelectronics: Understanding the processing, structure, and physical and electrical limits," *Journal of Applied Physics*, vol. 90, no. 5, pp. 2057–2121, Sep. 2001.

[5] G. K. Celler and S. Cristoloveanu, "Frontiers of silicon-on-insulator," *Journal of Applied Physics*, vol. 93, no. 9, pp. 4955–4978, May 2003.

[6] H. S. P. Wong, K. K. Chan, and Y. Taur, "Self-Aligned(Top and Bottom)Double-Gate MOSFET with a 25 nm Thick Silicon Channel," in *International Electron Device Meeting*, 1997, pp. 427–430.

[7] X. Huang, W. C. Lee, C. Kuo, D. Hisamoto, L. Chang, J. Kedzierski, E. Anderson, H. Takeuchi, Y. K. Choi, K. Asano, V. Subramanian, T. J. King, J. Bokor, and C. Hu, "Sub 50-nm FinFET:PMOS," in *International Electron Device Meeting*, 1999, pp. 67–70.

[8] R. Martel, T. Schmidt, H. R. Shea, T. Hertel, and P. Avouris, "Single- and multi-wall carbon nanotube field-effect transistors," *Applied Physics Letters*, vol. 73, no. 17, pp. 2447–2449, Oct. 1998.

[9] A. Javey, M. Shim, and H. Dai, "Electrical properties and devices of a large-diameter single-walled carbon nanotubes," *Applied Physics Letters*, vol. 80, no. 6, pp. 1064–1066, Feb. 2002.

[10] C. Zhou, J. Kong, and H. Dai, "Electrical measurements of individual semiconducting single-walled carbon nanotubes of various diameters," *Applied Physics Letters*, vol. 76, no. 12, pp. 1597–1599, Mar. 2000.

[11] A. Bachtold, P. Hadley, T. Nakanishi, and C. Dekker, "Logic circuits with carbon nanotube transistors," *Science*, vol. 294, pp. 1317–1319, Nov. 2001.

[12] S. J. Wind, J. Appenzeller, R. Martel, V. Derycke, and P. Avouris, "Vertical scaling of carbon nanotube field-effect transistors using top gate electrodes," *Applied Physics Letters*, vol. 80, no. 20, pp. 3817–3819, May 2002.

[13] P. L. McEuen, M. Bockrath, D. H. Cobden, Y. G. Yoon, and S. G. Louie, "Disorder, pseudospins, and backscattering in carbon nanotubes," *Physical Review Letters*, vol. 83, no. 24, pp. 5098–5101, Dec. 1999.

[14] M. A. Kastner, "Artificial atoms," *Physics Today*, vol. 46, pp. 24–31, Jan. 1993.

[15] ——, "The single-electron transistor," *Reviews of Modern Physics*, vol. 64, no. 3, pp. 849–858, Jul. 1992.

[16] U.Meirav and E. B. Foxman, "Single-electron phenomena in semiconductors," *Semicond. Sci. Technol.*, vol. 11, pp. 255–284, 1996.

[17] R. C. Ashoori, "Electrons in artificial atoms," *Nature*, vol. 379, pp. 413–419, Feb. 1996.

[18] E. Leobandung, L. Guo, Y. Wang, and S. Y. Chou, "Observation of quantum effects and coulomb blockade in silicon quantum-dot transistors at temperatures over 100 K," *Applied Physics Letters*, vol. 67, no. 7, pp. 938–940, Aug. 1995.

[19] K. Matsumoto, M. Ishii, K. Segawa, and Y. Oka, "Room temperature operation of a single electron transistor made by the scanning tunneling microscope nanooxidation process for the TiO_x/Ti system," *Applied Physics Letters*, vol. 68, no. 1, pp. 34–36, Jan. 1996.

[20] D. L. Klein, R. Roth, A. K. L. Lim, A. P. Alivisatos, and P. L. McEuen, "A single-electron transistor made from cadmium selenide nanocrystal," *Nature*, vol. 389, pp. 699–701, Oct. 1997.

[21] L. Guo, E. Leobandung, and S. Y. Chou, "A Silicon Single-Electron Transistor Memory Operating at Room Temperature," *Science*, vol. 275, pp. 649–651, Jan. 1997.

[22] S. Datta, W. Tian, S. Hong, R. Reifenberger, J. I. Henderson, and C. P. Kubiak, "Current-Voltage Characteristics of Self-Assembled Monolayers by Scaning Tunneling Microscopy," *Physical Review Letters*, vol. 79, no. 13, pp. 2530–2533, Sep. 1997.

[23] M. A. Reed, C. Zhou, C. J. Muller, T. P. Burgin, and J. M. Tour, "Conductance of a Molecular Junction," *Science*, vol. 278, pp. 252–254, Oct. 1997.

[24] M. A. Reed, "Molecular-Scale Electronics," in *Proc. IEEE*, vol. 87, no. 4, Apr. 1999, pp. 652–658.

[25] S. J. Tans, A. R. M. Verschueren, and C.Dekker, "Room-temperature transistor based on a single carbon nanotube," *Nature*, vol. 393, pp. 49–52, May 1998.

[26] K. Yano, T. Ishii, T. Sano, T. Mine, F. Murai, T. Hashimoto, T. Kobayashi, T. Kure, and K. Seki, "Single-Electron Memory for Giga-to-Tera bit Storage," in *Proc. IEEE*, vol. 87, no. 4, Apr. 1999, pp. 633–651.

[27] J. Watrous, "On one-dimensional quantum cellular automata," in *Proc. 1995 36th Annual Symposium on Foundations of Computer Science*, 1995, pp. 528–537.

[28] M. Monthioux and V. L. Kuznetsov, "Who should be given the credit for the discovery of carbon nanotubes?" *Carbon*, vol. 44, pp. 1621–1623, Aug. 2006.

[29] S. Iijima, "Helical microtubes of graphitic carbon," *Nature*, vol. 354, pp. 56–58, Nov. 1991.

[30] P. L. McEuen, M. S. Fuhrer, and H. Park, "Single-Walled Carbon Nanotube Electronics," *IEEE Transactions on Nanotechnology*, vol. 1, pp. 78–85, Mar. 2002.

[31] R. Saito, G. Dresselhaus, and M. S. Dresselhaus, *Physical Properties of Carbon Nanotubes*. London: Imperial College Press, 1998.

[32] "Multiwall carbon nanotbubes," http://physicsworld.com/cws/article/print/606.

[33] "MODELS OF NANOTUBES," http://physicsworld.com/cws/article/print/1761.

[34] S. J. Tans, M. H. Devoret, H. Dai, A. Thess, R. E. Smalley, L. J. Geerligs, and C. Dekker, "Individual single-wall carbon nanotubes as quantum wires," *Nature*, vol. 386, pp. 474–477, Apr. 1997.

[35] M. Bockrath, D. H. Cobden, P. L. McEuen, N. G. Chopra, A. Zettl, A. Thess, and R. E. Smalley, "Single-Electron Transport in Ropes of Carbon Nanotubes," *Science*, vol. 275, pp. 1922–1925, Mar. 1997.

[36] S. J. Wind, M. Radosavljević, J. Appenzeller, and P. Avouris, "Transistor structures for the study of scaling in carbon nanotubes," *J. Vac. Sci. Technol. B*, vol. 21(6), pp. 2856–2859, Nov./Dec. 2003.

[37] J. Kong, E. Yenilmez, T. W. Tombler, W. Kim, and H. Dai, "Quantum Interference and Ballistic Transmission in Nanotube Electron Waveguides," *Pysical Review Letters*, vol. 87, no. 10, p. 106801, Sep. 2001.

[38] J. Park, S. Rosenblatt, Y. Yaish, V. Sazonova, H. Ütünel, S. Braig, T. A. Arias, P. W. Brouwer, and P. J. McEuen, "Electron-Phonon Scattering in Metallic Single-Walled Carbon Nanotubes," *Nano Letters*, vol. 4, no. 3, pp. 517–520, Feb. 2004.

[39] S. Datta, *Electronic Transport in Mesoscopic Systems*. Cambridge, UK: Cambridge University Press, 1995.

[40] Z. Yao, C. L. Kane, and C. Dekker, "High-Field Electrical Transport in Single-Wall Carbon Nanotubes," *Physical Review Letters*, vol. 84, no. 13, pp. 2941–2944, Mar. 2000.

[41] P. J. Burke, "Lüttinger liquid theory as a model of the gigahertz electrical properties of carbon nanotubes," *IEEE Transactions on Nanotechnology*, vol. 1, no. 3, pp. 129–144, Sep. 2002.

[42] G. W. Hanson, "Fundamental Transmitting Properties of Carbon Nanotube Antennas," *IEEE Transactions on Antennas and Propagation*, vol. 53, no. 11, pp. 3426–3435, Nov. 2005.

[43] M. V. Shuba and S. A. Maksimenko, "Electromagnetic wave propagation in an almost circular bundle of closely packed metallic carbon nanotubes," *Physical Review B*, vol. 76, no. 155407, Oct. 2007.

[44] S. Ilani, L. A. K. Donev, M. Kindermann, and P. L. McEuen, "Measurement of the quantum capacitance of interacting electrons in carbon nanotubes," *nature physics*, vol. 2, pp. 687–691, Oct. 2006.

[45] M. Zhang, X. Huo, P. C. H. Chan, Q. Liang, and Z. K. Tang, "Radio-frequency transmission properties of carbon nanotubes in a field-effect transistor configuration," *IEEE Electron Device Letters*, vol. 27, no. 8, pp. 668–670, Aug. 2006.

[46] J. J. Plombon, K. P. O'Brien, F. Gstrein, V. M. Dubin, and Y. Jiao, "High-frequency electrical properties of individual and bundled carbon nanotubes," *Applied Physics Letters*, vol. 90, no. 063106, Feb. 2007.

[47] F. Rodriguez-Morales, R. Zannoni, J. Nicholson, M. Fischetti, K. S. Yngvesson, and J. Appenzeller, "Direct and heterodyne detection of microwave in a metallic single wall carbon nanotube," *Applied Physics Letters*, vol. 89, no. 083502, Aug. 2006.

[48] H. W. C. Postma, M. de Jonge, Z. Yao, and C. Dekker, "Electrical transport through carbon nanotube junctions created by mechanical manipulation," *Physical Review B*, vol. 62, no. 16, pp. 653–656, Oct. 2000.

[49] K. S. Yngvesson, "Very wide bandwidth hot electron bolometer heterodyne detectors based on single-walled carbon nanotubes," *Applied Physics Letters*, vol. 87, no. 043503, Jul. 2005.

[50] S. Yngvesson, *Microwave Semiconductor Devices*. Kluwer Academic Publishers, 1991.

[51] F. Arams, C. Allen, B. Peyton, and E. Sard, "Millimeter Mixing and Detection in Bulk $InSb$," in *Proc. IEEE*, vol. 54, 1966, pp. 612–622.

[52] F. Arams, "Infrared to millimeter wavelength detectors," *Dedham, Mass. : Artech House, 1973*, 1973.

[53] J. X. Yang, "*AlGaAs/GaAs* Two Dimensional Electron Gas Devices: Applications in Millimeter and Submillimeter Waves," Ph.D. dissertation, University of Massachusetts Amherst, U.S.A., 1992.

[54] H. Ekström, B. S. Karasik, E. L. Kollberg, and K. S. Yngvesson, "Conversion Gain and Noise of Niobium Superconducting Hot-Electron-Mixers," *IEEE Transactions on Microwave Theory and Techniques*, vol. 43, pp. 938–947, Apr. 1995.

[55] P. L. Richards, "Bolometers for infrared and millimeter waves," *Journal of Applied Physics*, vol. 76, Jul. 1994.

[56] J. Kim, H. So, N. Kim, J. Kim, and K. Kang, "Microwave response of individual multiwall carbon nanotubes," *Physical Review B*, vol. 70, no. 15, p. 153402, 2004.

[57] S. Rosenblatt, H. Lin, V. Sazonova, S. Tiwari, and P. L. McEuen, "Mixing at 50 GHz using a single-walled carbon nanotube transistor," *Applied Physics Letters*, vol. 87, no. 153111, Oct. 2005.

[58] A. A. Pesetski, J. E. Baumgardner, E. Folk, J. X. Przybysz, J. D. Adam, and H. Zhang, "Carbon nanotube field-effect transistor operation at microwave frequencies," *Applied Physics Letters*, vol. 88, no. 113103, Mar. 2006.

[59] M. Tarasov, "Carbon nanotube bolometers," *Applied Physics Letters*, vol. 90, no. 163503, Apr. 2007.

[60] M. E. Itkis, F. Borondics, A. Yu, and R. C. Haddon, "Bolometric Infrared Photoresponse of Suspended Single-Walled Carbon Nanotube Films," *Science*, vol. 312, pp. 413–416, Apr. 2006.

[61] C. Rutherglen and P. Burke, "Carbon Nanotube Radio," *Nano Letters*, vol. 7, no. 11, pp. 3296–3299, Sep. 2007.

[62] K. Jensen, J. Weldon, H. Garcia, and A. Zettl, "Nanotube Radio," *Nano Letters*, vol. 7, no. 11, pp. 3508–3511, Oct. 2007.

[63] E. Gerecht, C. F. Musante, Y. Zhuang, S. Yngvesson, T. Goyette, J. Dickinson, J. Waldman, P. A. Yagoubov, G. N. Gol'tsman, B. M. Voronov, and E. M. Gershenzon, "NbN Hot Electron Bolometric Mixers – A New Technology for Low Noise Thz Receivers," *IEEE Transactions on Microwave Theory and Techniques*, vol. 47, no. 12, pp. 2519–2527, Dec. 1999.

[64] S. Cherednichenko, M. Kroug, P. Khosropanah, A. Adam, H. Merkel, E. Kollberg, D. Loudkov, B. Voronov, G. N. Gol'tsman, H. W. Hübers, and H. Richter, "1.6 THz heterodyne receiver for the far infrared space telescope," *Physica C*, vol. 372, Aug. 2002.

[65] E. Gerecht, S. Yngvesson, J. Nicholson, Y. Zhuang, F. Rodriguez-Morales, X. Zhao, D. Gu, R. Zannoni, M. Coulombe, J. Dickinson, T. Goyette, B. Gorveatt, J. Waldman, P. Khosropanah, C. Groppi, A. Hedden, D. Golish, C. Walker, J. Kooi, R. Chamberlin, A. Stark, C. Martin, R. Stupak, N. Tothill, and A. Lane, "Deployment of trend - a low-noise receiver user instrument at 1.25 thz to 1.5 thz for ast/ro at the south pole," in *14th Int. Space Terahertz Technol. Symp.*, Tucson, AZ, U.S.A., 2003, pp. 179–188.

[66] G. F. Close and H. S. P. Wong, "Measurability issues in the Radio-Frequency Characterization of Carbon Nanotubes," in *Nanotechnology,2006. IEEE-NANO 2006. Sixth IEEE conference on,2006.*, vol. 1, Jun. 2006, pp. 266–269.

[67] A. J. Kerecman, "THE TUNGSTEN – P TYPE SILICON POINT CONTACT DIODE," *Microwave Symposium Digest, G-MTT International*, vol. 73, pp. 30–34, Jun. 1973.

[68] J. W. Fleming, "High-Resolution Submillimeter-Wave Fourier-Transform Spectrometry of Gases," *IEEE Transactions on microwave theory and techniques*, vol. 22, no. 12, pp. 1023–1025, Dec. 1974.

[69] J. Kong, A. M. Cassell, and H. Dai, "Chemical vapor deposition of methane for single-walled carbon nanotubes," *Chemical Physics Letters*, vol. 292, pp. 567–574, Jun. .1998.

[70] J. Kong, H. T. Soh, A. M. Cassell, C. F. Quate, and H. Dai, "Synthesis of individual single-walled carbon nanotubes on patterned silicon wafers," *Nature*, vol. 395, pp. 878–881, Oct. 1998.

[71] Y. S. Park, K. S. Kim, H. J. Jeong, W. S. Kim, J. M. Moon, K. H. An, D. J. Bae, Y. S. Lee, G.-S. Park, and Y. H. Lee, "Low pressure synthesis of single-walled carbon nanotubes by arc discharge," *Synthetic Metal*, vol. 126, pp. 245–251, 2002.

[72] "Cheap tubes, Inc., Brattleboro, VT."

[73] T. Guo, P. Nikolaev, A. G. Rinzler, D. TomBnek, D. T. Colbert, and R. E. Smalley, "Self-assembly of tubular fullerenes," *J. Phys. Chem.*, vol. 99, pp. 10 694–10 697, 1995.

[74] T. Guo, P. Nikolaev, A. Thess, D. T. Colbert, and R. E. Smalley, "Catalytic growth of single-walled nanotubes by laser vaporization," *Chemical Physics Letters*, vol. 243, pp. 49–54, Sep. 1995.

[75] A. Thess, R. Lee, P. Nikolaev, H. Dai, P. Petit, J. Robert, C. Xu, Y. H. Lee, S. G. Kim, A. G. Rinzler, D. T. Colbert, G. E. Scuseria, D. Tomanek, J. E. Fischer, and R. E. Smalley, "Crystalline Ropes of Metallic Carbon Nanotubes," *Science*, vol. 273, pp. 483–487, July 1996.

[76] Y. Mushiake, "Self-Complementary Antennas," *IEEE Antennas and Propagation Magazine*, vol. 34, no. 6, pp. 23–29, Dec. 1992.

[77] J. Li, Q. Zhang, D. Yang, and J. Tian, "Fabrication of carbon nanotube field effect transistors by AC dielectrophoresis method," *Carbon*, vol. 42, no. 11, pp. 2263–2267, 2004.

[78] N. Peng, Q. Zhang, J. Li, and N. Liu, "Influences of ac electric field on the spatial distribution of carbon nanotubes formed between electrodes," *Journal of Applied Physics*, vol. 100, no. 024309, 2006.

[79] L. Dong, V. Chirayos, J. Bush, J. Jiao, V. M. Dubin, R. V. Chebian, Y. Ono, J. F. C. Jr., and B. D. Ulrich, "Floating-Potential Dielectrophoresis-Controlled Fabrication of Single-Carbon-Nanotube Transistors and Their Electrical Properties," *Journal of Physical Chemistry B*, vol. 109, pp. 13 148–13 153, 2005.

[80] F. Rodriguez-Moralez, "Modeling and Measured Performance of Integrated Terahertz HEB Receivers and Focal Plane Arrays," Ph.D. dissertation, University of Massachusetts Amherst, U.S.A., 2007.

[81] M. Ji, "Lens Coupled Printed Antenna Characterization," Master's thesis, University of Massachusetts Amherst, U.S.A., 2001.

[82] X. Zhao, "Integrated Antennas for Thz Hot Electron Bolometer Mixers," Master's thesis, University of Massachusetts Amherst, U.S.A., 2005.

[83] A. Maestrini, J. Ward, H. Javadi, E. Schlecht, G. Chattopadhyay, F. Maiwald, N. Erickson, and I. Mehdi, "A 1.7-1.9 THz Local Oscillator Source,," *IEEE Microw. Wireless Comp. Lett.*, vol. 14, pp. 253–255, Jun. 2004.

[84] J. Hesler, D. Porterfield, W. Bishop, T. Crowe, A. Baryshev, R. Hesper, and J. Baselmans, "Development and Characterization of an Easy-to-Use THz Source," in *Proc. 16th Int. Space Terahertz Technology Symp.*, Gothenburg, Sweden, May. 2005.

[85] A. Maestrini, J. Ward, H. Javadi, C. Tripon-Canseliet, J. Gill, G. Chattopadhyay, E. Schlecht, and I. Mehdi, "Local Oscillator Chain for 1.55 to 1.75 THz With 100-μw Peak Power," *IEEE Microw. Wireless Comp. Lett.*, vol. 15, pp. 871–873, Dec. 2005.

[86] R. Hall, J. Racette, and H. Ehrenreich, "Direct Observation of Polarons and Phonons During Tunneling in Group 3-5 Semiconductor Junctions," *Physical Review Letters*, vol. 4, no. 9, pp. 456–458, 1960.

[87] M. Bockrath, D. Cobden, J. Lu, P. McEuen, A. Rinzler, R. Smalley, and L. Balents, "Luttinger-liquid behaviour in carbon nanotubes," *Nature*, vol. 397, no. 6720, pp. 598–601, 1999.

[88] S. Li, Z. Yu, S. Yen, W. Tang, and P. Burke, "Carbon nanotube transistor operation at 2.6 GHz," *Nano Lett*, vol. 4, no. 4, pp. 753–756, 2004.

[89] S. Langley, *The Bolometer*. American Journal of Science, 1898.

[90] P. Richards, J. Clarke, R. Leoni, P. Lerch, S. Verghese, M. Beasley, T. Geballe, R. Hammond, P. Rosenthal, and S. Spielman, "Feasibility of the high T superconducting bolometer," *Applied Physics Letters*, vol. 54, p. 283, 1989.

[91] J. Yang, F. Agahi, D. Dai, C. Musante, W. Grammer, K. Lau, and K. Yngvesson, "Wide-bandwidth electron bolometric mixers: a 2DEG prototype andpotential for low-noise THz receivers," *Microwave Theory and Techniques, IEEE Transactions on*, vol. 41, no. 4, pp. 581–589, 1993.

[92] M. Lee, L. Pfeiffer, and K. West, "Ballistic cooling in a wideband two-dimensional electron gas bolometric mixer," *Applied Physics Letters*, vol. 81, p. 1243, 2002.

[93] N. Mingo and D. Broido, "Carbon Nanotube Ballistic Thermal Conductance and Its Limits," *Physical Review Letters*, vol. 95, no. 9, p. 96105, 2005.

[94] C. Kittel, *Introduction to Solid State Physics*, 8th ed. Hoboken, N.J. : John Wiley and Sons, 2005.

[95] R. Zannoni, "Bias II: Improving stability in terahertz imaging," Master's thesis, University of Massachusetts Amherst, U.S.A., 2008.

[96] M. Kobrinsky, S. Chakravarty, D. Jiao, M. Harmes, S. List, and M. Mazumder, "Experimental validation of crosstalk simulations for on-chip interconnects using S-parameters," *Advanced Packaging, IEEE Transactions on [see also Components, Packaging and Manufacturing Technology, Part B: Advanced Packaging, IEEE Transactions on]*, vol. 28, no. 1, pp. 57–62, 2005.

[97] D. Pozar *et al.*, *Microwave engineering*. Wiley New York, 1998.

[98] A. Tselev, M. Woodson, C. Qian, and J. Liu, "Microwave Impedance Spectroscopy of Dense Carbon Nanotube Bundles," *Nano Lett*, vol. 8, no. 1, pp. 152–156, 2008.

[99] P. Rice, T. Wallis, S. Russek, and P. Kabos, "Broadband Electrical Characterization of Multiwalled Carbon Nanotubes and Contacts," *Nano Lett*, vol. 7, no. 4, pp. 1086–1090, 2007.

[100] J. Cao, Q. Wang, D. Wang, and H. Dai, "Suspended Carbon Nanotube Quantum Wires with Two Gates," *Small*, vol. 1, no. 1, pp. 138–141, 2005.

[101] W. Grammer, "CHARACTERIZATION OF THE TWO-DIMENSIONAL ELECTRON GAS DEVICE (2DEG) AT 77K," Master's thesis, University of Massachusetts Amherst, U.S.A., 1992.

[102] E. Pop, D. Mann, K. Goodson, and H. Dai, "Electrical and thermal transport in metallic single-wall carbon nanotubes on insulating substrates," *Journal of Applied Physics*, vol. 101, p. 093710, 2007.

[103] H. Maune, H. Chiu, and M. Bockrath, "Thermal resistance of the nanoscale constrictions between carbon nanotubes and solid substrates," *Applied Physics Letters*, vol. 89, p. 013109, 2006.